ADVANCED ENERGY MATERIALS
www.advenergymat.de

High Thermoelectric Performance in p-type Polycrystalline Cd-doped SnSe Achieved by a Combination of Cation Vacancies and Localized Lattice Engineering

Xiaolei Shi, Angyin Wu, Tianli Feng, Kun Zheng, Weidi Liu, Qiang Sun, Min Hong, Sokrates T. Pantelides, Zhi-Gang Chen, and Jin Zou**

Herein, a high figure of merit (*ZT*) of ≈1.7 at 823 K is reported in p-type polycrystalline Cd-doped SnSe by combining cation vacancies and localized-lattice engineering. It is observed that the introduction of Cd atoms in SnSe lattice induce Sn vacancies, which act as p-type dopants. A combination of facile solvothermal synthesis and fast spark plasma sintering technique boosts the Sn vacancy to a high level of ≈2.9%, which results in an optimum hole concentration of ≈2.6 × 10^{19} cm^{-3} and an improved power factor of ≈6.9 μW cm^{-1} K^{-2}. Simultaneously, a low thermal conductivity of ≈0.33 W m^{-1} K^{-1} is achieved by effective phonon scattering at localized crystal imperfections, as observed by detailed structural characterizations. Density functional theory calculations reveal that the role of Cd atoms in the SnSe lattice is to reduce the formation energy of Sn vacancies, which in turn lower the Fermi level down into the valence bands, generating holes. This work explores the fundamental Cd-doping mechanisms at the nanoscale in a SnSe matrix and demonstrates vacancy and localized-lattice engineering as an effective approach to boosting thermoelectric performance. The work provides an avenue in achieving high-performance thermoelectric properties of materials.

1. Introduction

By converting heat into electricity, thermoelectric materials provide a potential solution to the world energy crisis as well as to environmental issues that arise from fossil fuels.[1–4] The energy conversion efficiency of thermoelectric materials is measured by the dimensionless figure of merit $ZT = S^2\sigma T/\kappa = S^2\sigma T/(\kappa_e + \kappa_l)$,[3] where σ, S, $S^2\sigma$, T, κ, κ_e, and κ_l are the electric conductivity, the Seebeck coefficient, the power factor, the absolute temperature, the total thermal conductivity, and the electronic and lattice thermal conductivities,[5,6] respectively. To date, two major strategies for achieving high *ZT* are optimizing the power factor and reducing κ_l by band and structural engineering, respectively.[7,8]

Stannous selenide (SnSe) has attracted much attention because of its great potential in realizing high-performance, low-toxic, and low-cost thermoelectric devices.[3,9–13] Spectacularly high peak *ZT*s of ≈2.6 at 923 K[14] and ≈2.8 at 773 K[15] were reported in p-type and n-type SnSe single crystals, owing to their high power factor and remarkably low thermal conductivity along specified crystal directions.[14,15] However, due to the special demands of crystal-growth techniques, prospective high cost for production, and undesirable mechanical properties,[10,16] SnSe single

X.-L. Shi, A.-Y. Wu, W.-D. Liu, Q. Sun, Prof. Z.-G. Chen, Prof. J. Zou
Materials Engineering
the University of Queensland
Brisbane, QLD 4072, Australia
E-mail: zhigang.chen@uq.edu.au, zhigang.chen@usq.edu.au; j.zou@uq.edu.au

Dr. T. Feng, Prof. S. T. Pantelides
Department of Physics and Astronomy and
Department of Electrical Engineering and Computer Science
Vanderbilt University
Nashville, TN 37235, USA

Dr. T. Feng, Prof. S. T. Pantelides
Materials Science and Technology Division
Oak Ridge National Laboratory
Oak Ridge, TN 37831, USA

Prof. K. Zheng
Beijing Key Lab of Microstructure and Property of Solids
Institute of Microstructure and Properties of Advanced Materials
Beijing University of Technology
Beijing 100124, China

Dr. M. Hong, Prof. Z.-G. Chen
Centre for Future Materials
University of Southern Queensland
Springfield central, QLD 4300, Australia

Prof. J. Zou
Centre for Microscopy and Microanalysis
the University of Queensland
Brisbane, QLD 4072, Australia

The ORCID identification number(s) for the author(s) of this article can be found under https://doi.org/10.1002/aenm.201803242.

DOI: 10.1002/aenm.201803242

 © 2019 WILEY-VCH Verlag GmbH & Co. KGaA, Weinheim

crystals are not well-suited for thermoelectric devices and have considerable limitations for industrial scale-up.[15,17,18] Besides, there are critical controversies on the reported high *ZT*s in single-crystal SnSe[19,20] because the mass densities of experimental samples are much smaller than the theoretical density of SnSe.[20] In this context, polycrystalline SnSe has become a promising alternative candidate.[3,7,21,22] To improve the relatively low power factor and reduce the high thermal conductivity of polycrystalline SnSe,[17] three major strategies including doping,[3,7,23] multiphase alloying,[3,24] and micro/nanoscale texturing[3,25] have been employed. The peak *ZT*s have been improved from ≈0.5 to ≈1.5 before 850 K.[3] Considering that SnSe is easy to volatilize Se and become unstable at higher temperature, it has been a challenge to improve *ZT* even higher to $ZT > 1.5$ before 850 K, which is necessary for device applications.[18,26,27]

In order to achieve high-*ZT* polycrystalline SnSe, a key step is to tune an appropriate carrier concentration *n*, which optimizes the electrical transport properties.[3,28] In solution-based synthesis routes such as hydrothermal[3] and solvothermal[3,29] syntheses, the cation and/or anion vacancy concentrations can be controlled by tuning the synthesis parameters such as the stoichiometric ratio of precursors, synthesis temperature, synthesis pressure, and potential of hydrogen (pH) level according to the reaction kinetics and/or thermodynamics.[3,30] "Vacancy engineering" is an effective strategy to tune *n* and ultimately enhance *ZT*s of polycrystalline SnSe because Sn vacancies are known to dope SnSe p-type, and Se vacancies are known to dope SnSe n-type.[3] For p-type SnSe, however, to achieve an optimal Sn vacancy level has historically been difficult.[31–34] A previous study found that heavy Na^+ doping achieved a high maximum Sn vacancy level of ≈2%, which induces a hole carrier concentration $p = \approx 1.5 \times 10^{19}$ cm^{-3} and a relatively high $ZT = \approx 1.36$ at 823 K.[7] However, such *ZT* is still not optimal since 2% Sn vacancies are not sufficient for the desired *p*,[7] while higher Na^+ concentration could not further increase the Sn vacancy concentration because Na^+ does not act as a dopant but only triggers Sn-vacancy formation.[7] Therefore, it is necessary to seek an appropriate dopant that has stable +2 valence state (same as Sn^{2+}) as well as a different atomic/ionic size because the size difference can result in lattice heterogeneity (dilatation or contraction),[21,23] which can weaken the bonding ability of Sn and Se and expand the maximum cation vacancy level. Meanwhile, such lattice heterogeneity can also reduce κ_l by increasing the phonon scattering with nanoscale crystal imperfections such as point defects and lattice distortions.[31–34]

In this study, we choose Cd as dopant to meet the requirements listed above since Cd is an ideal candidate with stable 2+ valence state and different atomic/ionic size (0.166/0.095 nm) compared to Sn/Sn^{2+} (0.151/0.112 nm).[35] We design a facile solvothermal synthesis route with a fast spark plasma sintering (SPS) technique to fabricate polycrystalline Cd-doped SnSe, as shown in **Figure 1**a,b, respectively. Comprehensive compositional investigations including X-ray photoelectron spectroscopy (XPS), electron probe micro-analyzer (EPMA), and energy dispersive spectroscopy (EDS) demonstrated that our Cd-doping achieved a high cation vacancy concentration of ≈2.9%, leading to an increased $p = \approx 2.6 \times 10^{19}$ cm^{-3}, and in turn an improved $S^2\sigma$ of ≈6.9 μW cm^{-1} K^{-2} at 823 K. Besides, extensive structural and morphological characterizations including XPS, X-ray diffraction (XRD), scanning electron microscopy (SEM), and transmission electron microscopy (TEM) with spherical aberration-corrected scanning TEM (Cs-corrected STEM) indicate that the Cd-doping can result in localized crystal imperfections including localized lattice distortions and strains, dislocations, and nanoscale vacancy domains (illustrated in Figure 1c). These defects lead to a low κ_l of ≈0.33 W m^{-1} K^{-1} and in turn a high peak *ZT* of ≈1.7 at 823 K, which is a record value at this temperature compared with reported studies, as shown in Figure 1d. Furthermore, a competitive *ZT* of ≈1.3 at 773 K before the phase transition temperature (800 K) and a high average *ZT* of 0.84 for the entire temperature range can be simultaneously achieved, showing that the polycrystalline Cd-doped SnSe has considerable potential for device applications. In fact, this study serves as an exploration of the fundamental Cd-doping mechanisms at the nanoscale in a SnSe matrix, and describes a novel concept to realize high *ZT* in polycrystalline SnSe.

2. Results and Discussion

A suitably large *p* and low κ are vital for achieving high *ZT* for polycrystalline SnSe. To predict an suitable *p* for high *ZT*, we use a single parabolic band (SPB) model[42–45] to study *p*-dependent *ZT* at $T = 823$ K with a fixed κ_l of 0.4 W m^{-1} K^{-1}, as shown in **Figure 2**a (details can be seen in 1 in the Supporting Information). It is seen that $p = \approx 3.0 \times 10^{19}$ cm^{-3} can contribute to a peak *ZT* of ≈1.4, which is competitive to the currently reported polycrystalline SnSe.[3] In terms of thermal conductivity κ, since lattice vibrations (κ_l) contribute more than 50% to the total κ in polycrystalline SnSe under 850 K,[7,14,21] minimizing κ_l plays a significant role in lowering κ. We have studied *p*-dependent *ZT* at $T = 823$ K with different κ_l values. As shown in Figure 2b, a high peak *ZT* of ≈1.85 at 823 K can be obtained when κ_l is reduced to 0.2 W m^{-1} K^{-1}, which is close to its minimum value of 0.26 W m^{-1} K^{-1}[46] calculated under the condition of full density along the *a*-axis.[3] Thus, it is possible to improve *ZT*s by appropriately tuning *p* and reducing κ_l.

To verify that Cd is an ideal candidate for improving the cation vacancy level, we first explore the solubility of Cd in SnSe, and then study the real compositions of Cd-doped SnSe with different doping concentrations, as shown in **Table 1**. In this study, we use $SnCl_2 \cdot 2H_2O$, Na_2SeO_3, and $CdCl_2$ as precursors to fabricate Cd-doped SnSe. We first define the mole percentage (*x*) of $CdCl_2$ in $SnCl_2 \cdot 2H_2O$. The nominal compositions of Cd-doped SnSe can then be described as $Sn_{1-x}Cd_xSe$, where the selected *x* values are 0% (no $CdCl_2$ added), 0.5%, 1%, 1.5%, 2%, 2.5%, 3%, and 3.5% as listed in Table 1. Through detailed EDS and EPMA studies, however, it was found that the real compositions of the synthesized products are different from the nominal compositions, as shown in Table 1. With increasing *x*, the cation vacancy level gradually increases until reaching a maximum value of 2.9%, from which a solubility limit of Cd (≈2.3%) is achieved when the real composition is

© 2019 WILEY-VCH Verlag GmbH & Co. KGaA, Weinheim

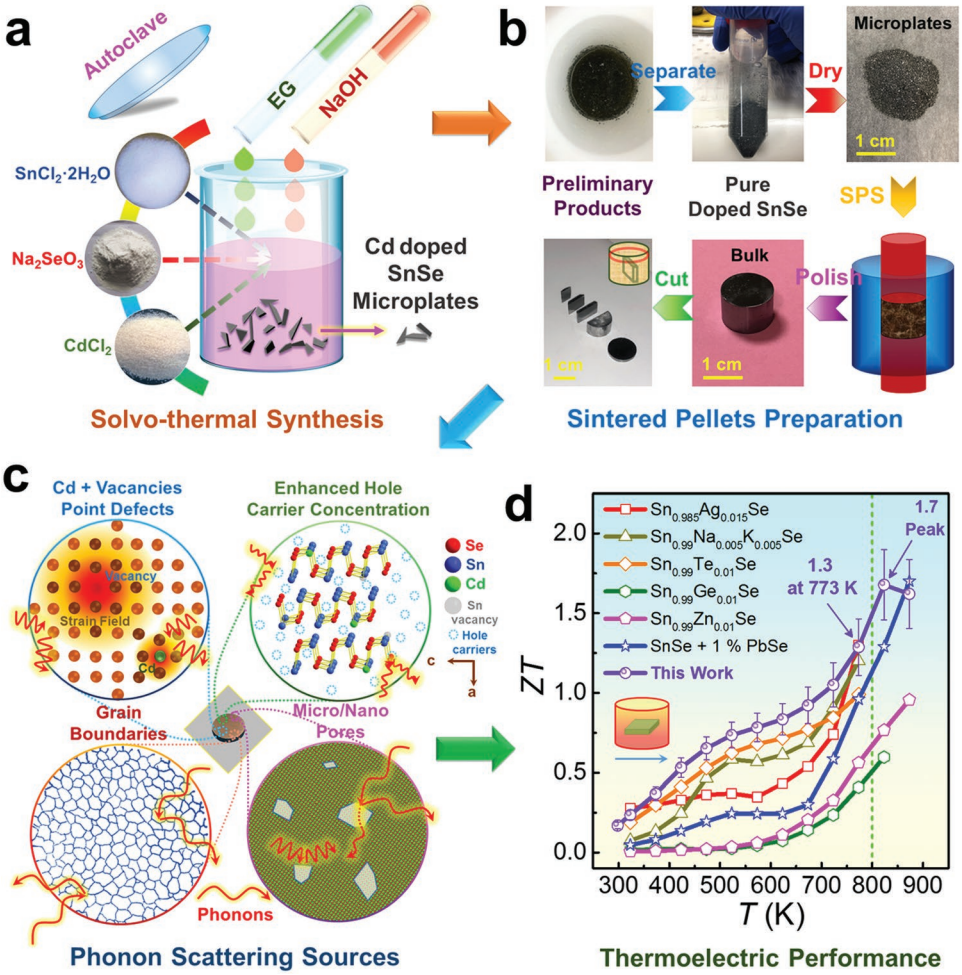

Figure 1. Illustrations of fabrication for our Cd-doped SnSe. a) Illustration of solvothermal synthesis; b) obtained Cd-doped SnSe products and subsequent sintering and cutting processes; c) phonon scattering sources observed in our pellets; and d) comparisons of achieved temperature-dependent *ZT* from our pellets with reported polycrystalline SnSe.[7,36–41]

$Sn_{0.948}Cd_{0.023}Se$. The instrumental error of EMPA is ≈0.1%, which demonstrates a high accuracy. These results indicate that Cd-doping has great potential for further increasing the cation vacancy level and hence the hole concentration as well as enhancing *ZT*.

To understand the impact of Cd atoms on Sn-vacancy formation, we performed density functional theory (DFT) calculations using SnSe supercells (256 atoms) with and without a Cd atom occupying the Sn site. The results are shown in Figure 2c. We find that the Sn-vacancy formation energy in pure SnSe lattice is about 1.63 eV (with respect to the chemical potential of Sn metal). After a Cd atom is introduced in the lattice by occupying a cation site, we recalculate the Sn-vacancy formation energies. We find that for the Sn atoms that are far from the Cd atom, the vacancy formation energy remains the same as expected. For the Sn atom that is nearest to the Cd atom, the vacancy formation energy is 1.50 eV, reducing by 0.13 eV, which is much larger than the room-temperature thermalization energy 0.026 eV. Therefore, the DFT results explicitly support the experimental observation that Cd dopants can facilitate the formation of Sn vacancies in SnSe. It should be mentioned that secondary phase (mainly CdSe) was identified after the doping level reached the Cd solubility in SnSe. However, the ultrasonic separation technique can effectively remove the secondary phase after the synthesis, as confirmed in Figure S2 in the Supporting Information.[7,21,23]

Table 1 indicates that Cd-doping can further improve the hole concentration *p*, but it is still unclear if such improvement is caused by the Cd atoms themselves or the induced Sn vacancies. To gain insight into the mechanism of the increase of the hole concentration, we have performed DFT calculations on the electronic band structure evolution for SnSe after Cd-doping with and without cation vacancy. **Figure 3**a–d) compares the calculated band structures of pure SnSe (with the supercell of $Sn_{128}Se_{128}$), Cd-doped SnSe without vacancies ($CdSn_{127}Se_{128}$), Cd-doped SnSe with one Sn vacancy ($CdSn_{126}Se_{128}$), and SnSe with one Sn vacancy without Cd, respectively. Figure 3e compares their corresponding density of states (DOSs). We find that the band structures and DOSs are almost identical with and without Cd replacing Sn, with the only difference being that the degenerate bands in the

 © 2019 WILEY-VCH Verlag GmbH & Co. KGaA, Weinheim

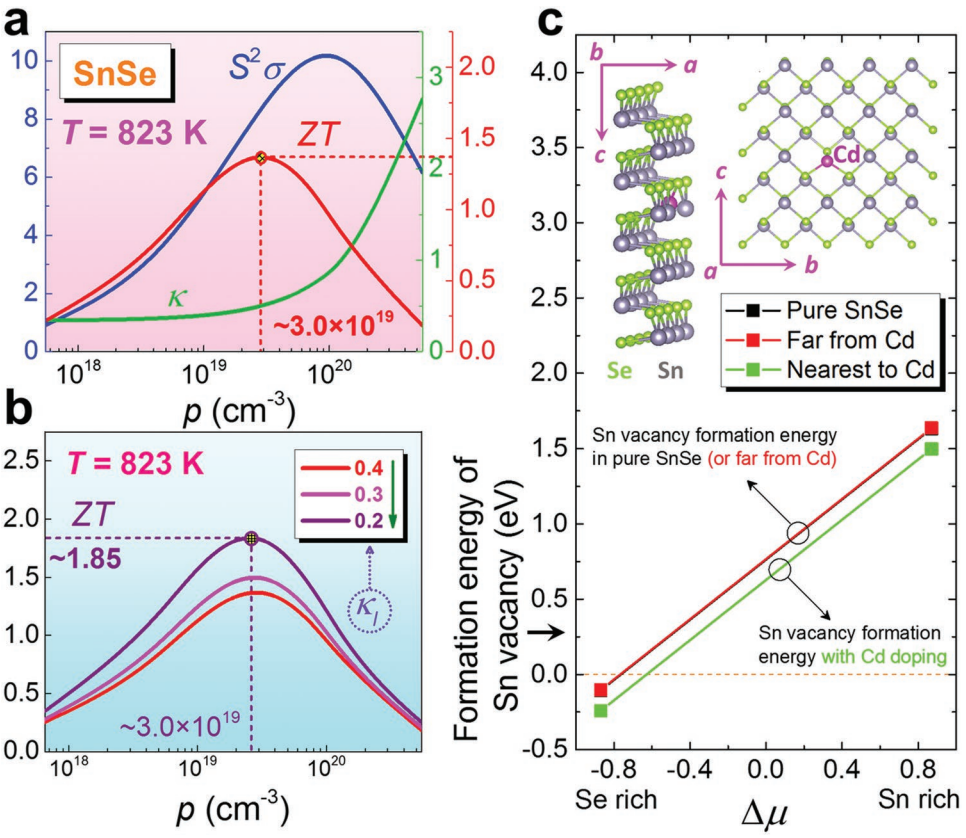

Figure 2. Calculated thermoelectric performance as a function of hole concentration and Sn-vacancy formation energy of SnSe. a) Calculated *p*-dependent *ZT* of polycrystalline SnSe at $T = 823$ K with a fixed κ_l of 0.4; b) improvement of *p*-dependent *ZT* via reducing κ_l; c) calculated results of Sn-vacancy formation energy before and after inducing Cd. The units of $S^2\sigma$ and κ (κ_l) are μW cm^{-1} K^{-2} and W m^{-1} K^{-1}, respectively.

perfect SnSe lattice split after a Cd atom is introduced. This difference originates from the breaking of the supercell symmetry by the Cd impurity and has negligible impact on the hole concentration.[3] In contrast, for the pure SnSe and Cd-doped SnSe with an extra Sn vacancy introduced, the Fermi level moves into the valence band, making the material a degenerate semiconductor with significantly increased hole concentration. Therefore, we conclude that it is the Sn vacancies rather than the Cd atoms that introduce holes in SnSe.

Table 1. Comparisons of measured real compositions via EPMA with nominal composition ($Sn_{1-x}Cd_xSe$). The corresponding vacancy rates (%) are also included.

Nominal composition [$Sn_{1-x}Cd_xSe$]	Real composition via EPMA	Vacancy [%]
SnSe	$Sn_{0.994}Se$	0.6
$Sn_{0.995}Cd_{0.005}Se$	$Sn_{0.984}Cd_{0.005}Se$	1.1
$Sn_{0.99}Cd_{0.01}Se$	$Sn_{0.976}Cd_{0.009}Se$	1.5
$Sn_{0.985}Cd_{0.015}Se$	$Sn_{0.966}Cd_{0.014}Se$	2.0
$Sn_{0.98}Cd_{0.02}Se$	$Sn_{0.957}Cd_{0.019}Se$	2.4
$Sn_{0.975}Cd_{0.025}Se$	$Sn_{0.948}Cd_{0.023}Se$	2.9
$Sn_{0.97}Cd_{0.03}Se$	$Sn_{0.948}Cd_{0.023}Se$	2.9
$Sn_{0.965}Cd_{0.035}Se$	$Sn_{0.948}Cd_{0.023}Se$	2.9

The role of Cd atoms is to increase the Sn vacancy concentration. More discussion about the effect of Cd-doping on conduction band of SnSe is shown in Figure S1 in the Supporting Information.

Figure 4a shows XRD results for our synthesized Cd-doped SnSe with different Cd-doping levels. It is clearly seen that all diffraction peaks can be indexed as orthorhombic-structured SnSe and a space group of *Pnma*, according to the JCPDS 48-1224 Standard Identification Card. The strongest diffraction peaks of 400* suggest our products contain significant (100) surfaces.[3,7,21,23] With increasing Cd-doping level, the other diffraction peaks such as 111* become weaker (refer to Figure S2b in the Supporting Information), indicating a strengthened anisotropy in the synthesized products.[3,7,21] Figure 4b shows magnified 400* diffraction peaks, and shows all peaks shifted toward higher 2θ angles, from $2\theta = 31.081°$ as the standard value, indicating a reduced lattice parameter *a*,[7,23,47] and in turn a shrunken unit cell derived from the Sn vacancies in SnSe.[7] Figure 4c,d shows the calculated lattice parameters *a*, *b*, *c*, and unit cell volume *V* as functions of the cation vacancy level given in Table 1. With increasing vacancy concentration, *a*, *b*, and *c* slightly decrease, resulting in a *V* shrinkage.[48]

Figure 5a shows a typical SEM image of the synthesized $Sn_{0.948}Cd_{0.023}Se$ microplates. The inset optical image shows that these microplates have silver-like metallic luster.[7]

© 2019 WILEY-VCH Verlag GmbH & Co. KGaA, Weinheim

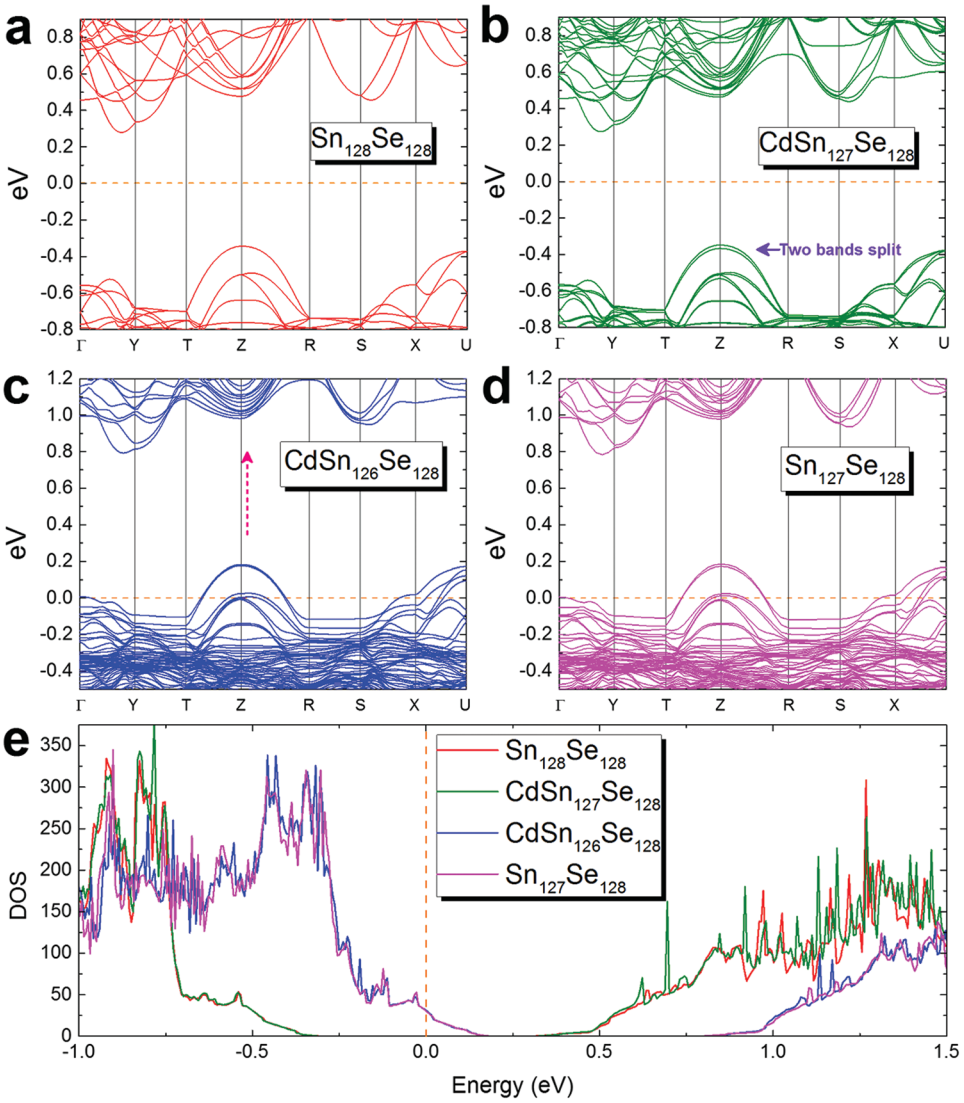

Figure 3. Band structures and DOS of SnSe. Comparisons of calculated electronic structures of a) pure SnSe ($Sn_{128}Se_{128}$); b) Cd-doped SnSe without vacancy ($CdSn_{127}Se_{128}$); c) Cd-doped SnSe with vacancy ($CdSn_{126}Se_{128}$); d) SnSe with vacancy ($Sn_{127}Se_{128}$); and e) Comparisons of corresponding DOS.

Compared with their undoped counterparts shown in Figure S3 in the Supporting Information, the most significant surfaces of Cd-doped microplates are also (100). But their average size (124.5 µm measured via Nano Measurer software with a sample capacity larger than 1000) is larger than their undoped counterparts (110.7 µm), indicating a strengthened anisotropy in these Cd-doped microplates,[3,7] which agrees with the XRD results shown in Figure 4a. Figure 5a also shows that the Cd-doped microplates tend to agglomerate to form a flower-like morphology.[21,25] Figure 5b shows a typical $Sn_{0.948}Cd_{0.023}Se$ microplate with a (100) surface, from which pores and slight crystal bent can be seen.[21] A typical pore is shown in the inset of Figure 5b in a magnified SEM image. Figure 5c shows one typical $Sn_{0.948}Cd_{0.023}Se$ microplate with lateral surfaces at a microscale as well as the corresponding atomic structure related to the surface features.

To further investigate the structural characteristics of the $Sn_{0.948}Cd_{0.023}Se$ microplates, detailed TEM characterization was performed. Figure 5d shows a [100] zone-axis TEM image for a typical $Sn_{0.948}Cd_{0.023}Se$ plate with the surface perpendicular to the electron beam. The inset corresponding to a selected area electron diffraction (SAED) pattern indicates that the plate has a typical orthorhombic structure with a (100) surface,[7,21] same as the undoped SnSe shown in Figure S4 in the Supporting Information. Figure 5e shows EDS results of Figure 5d, in which Cd has a uniform distribution at a microscale. Figure 5f is a high-resolution TEM (HRTEM) image circled in Figure 5d, showing local lattice distortions and dislocations (inset), which should be derived from the doped Cd with different atomic/ionic size of Sn.[21,23] Figure 5g is a STEM high-angle annular dark field (HAADF) image taken along the *a*-axis. The overlays in a normal area show Se atoms in green and Sn atoms in purple. The nonuniform structural contrast

 © 2019 WILEY-VCH Verlag GmbH & Co. KGaA, Weinheim

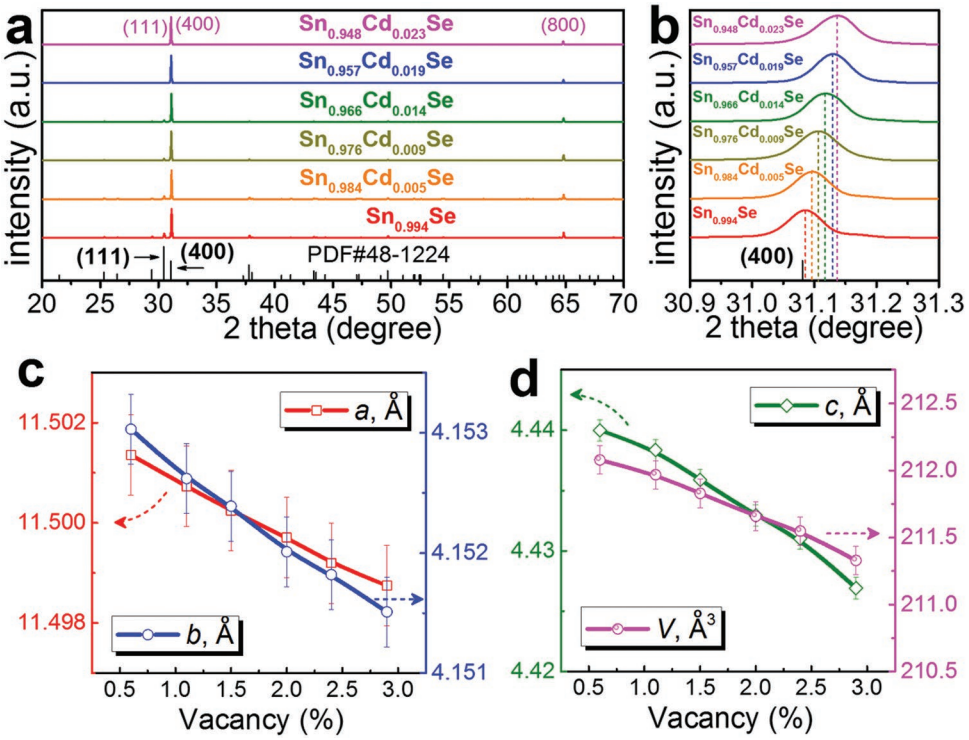

Figure 4. Structural characterizations of synthesized products. a) XRD results; b) enlarged 400* peaks to see the peak deviation. Achieved lattice parameters of c) *a*, *b*; d) *c* and *V* as a function of vacancy rate shown in Table 1.

suggests a lattice distortion, likely derived from the local elemental variation.[21,23] Figure 5h is the intensity line profile (taken along the dashed red line in Figure 5g, and shows different peak intensities between different areas, reflecting the local compositional variations (such as Cd replacement and cation vacancies).

We sintered the synthesized microplates into pellets to evaluate their thermoelectric performance along different directions, as illustrated in Figure 1b. Before the evaluation, we performed detailed structural and morphological characterizations on these pellets to confirm the structural and compositional features are stable after sintering. **Figure 6**a shows their XRD patterns (pure SnSe and $Sn_{0.948}Cd_{0.023}Se$) taken along both the ⊥ and // directions. Here "⊥" and "//" mean the directions perpendicular and parallel to the pressure of sintering, respectively. All diffraction peaks can be indexed as orthorhombic-structured SnSe, showing that the structural features remain with no extra phase observed.[21,23] Figure 6b magnifies the 111* and 400* peaks to reveal the peak-shifts. It shows the strongest 111* peaks for the sample taken along the // direction and the strongest 400* peaks along the ⊥ direction, demonstrating significant anisotropy in the pellets. Meanwhile, pure SnSe has a slightly stronger 111* peak than $Sn_{0.948}Cd_{0.023}Se$ along the ⊥ direction, indicating more significant anisotropy in $Sn_{0.948}Cd_{0.023}Se$ pellets.[23] Besides, the diffraction peaks taken from the $Sn_{0.948}Cd_{0.023}Se$ pellet move toward a higher 2θ than the peak from pure SnSe, similar to the XRD results shown in Figure 4a,b. Figure 6c shows XPS spectra of the $Sn_{0.948}Cd_{0.023}Se$ pellet with a full survey scan, demonstrating the existence of energy states for Se 3d, Sn 3d, and Cd 3d, indicating the successful doping of Cd. Except C and O, no other elements were identified. Figure 6d shows XPS spectra with a high-resolution scan for Cd $3d_{5/2}$ and Cd $3d_{3/2}$ (peaks at 405 and 412 eV, respectively), showing that only Cd^{2+} valence state exists in the system. These results indicate that the Cd atoms substituted Sn on Sn sites via doping, and there is no interstitial atom of Cd in the matrix of SnSe. The quantified at% of Cd fitted well with the proposed ≈2.3% of Cd.

Figure 7a is a typical SEM image of a polished surface from a $Sn_{0.948}Cd_{0.023}Se$ pellet (as inset optical image shows), in which a flat surface without any observable flaws can be seen, indicating a high compaction in the sintered pellets. Figure 7b shows corresponding EDS maps, indicating compositional stability after sintering. EPMA studies on the $Sn_{0.948}Cd_{0.023}Se$ pellet indicate that the Sn:Cd:Se ratio is 48.1:1.2:50.7, suggesting a stable composition of $Sn_{0.948}Cd_{0.023}Se$. Figure 7c,d are SEM images of pellets, fractured from different directions. Similar to the undoped SnSe (refer to Figure S5 in the Supporting Information), the distinct fracture features indicate an obvious anisotropy in the sintered pellets,[7,21] fitting well with the XRD results shown in Figure 6a,b. However, different from undoped SnSe pellets, faveolate structures can be occasionally found on the fractured grains of $Sn_{0.948}Cd_{0.023}Se$ pellets, as shown in magnified SEM images in the insets of Figure 7c,d. These specific structures might be derived from the crystal imperfections of the SnSe microplates caused by Cd-doping.[21] Figure 7e shows a TEM image of our sliced $Sn_{0.948}Cd_{0.023}Se$ pellet, from which obvious overlap of the grains can be observed. The inset HRTEM image shows a typical dislocation, indicating that the dislocation still existed after SPS. Figure 7f

© 2019 WILEY-VCH Verlag GmbH & Co. KGaA, Weinheim

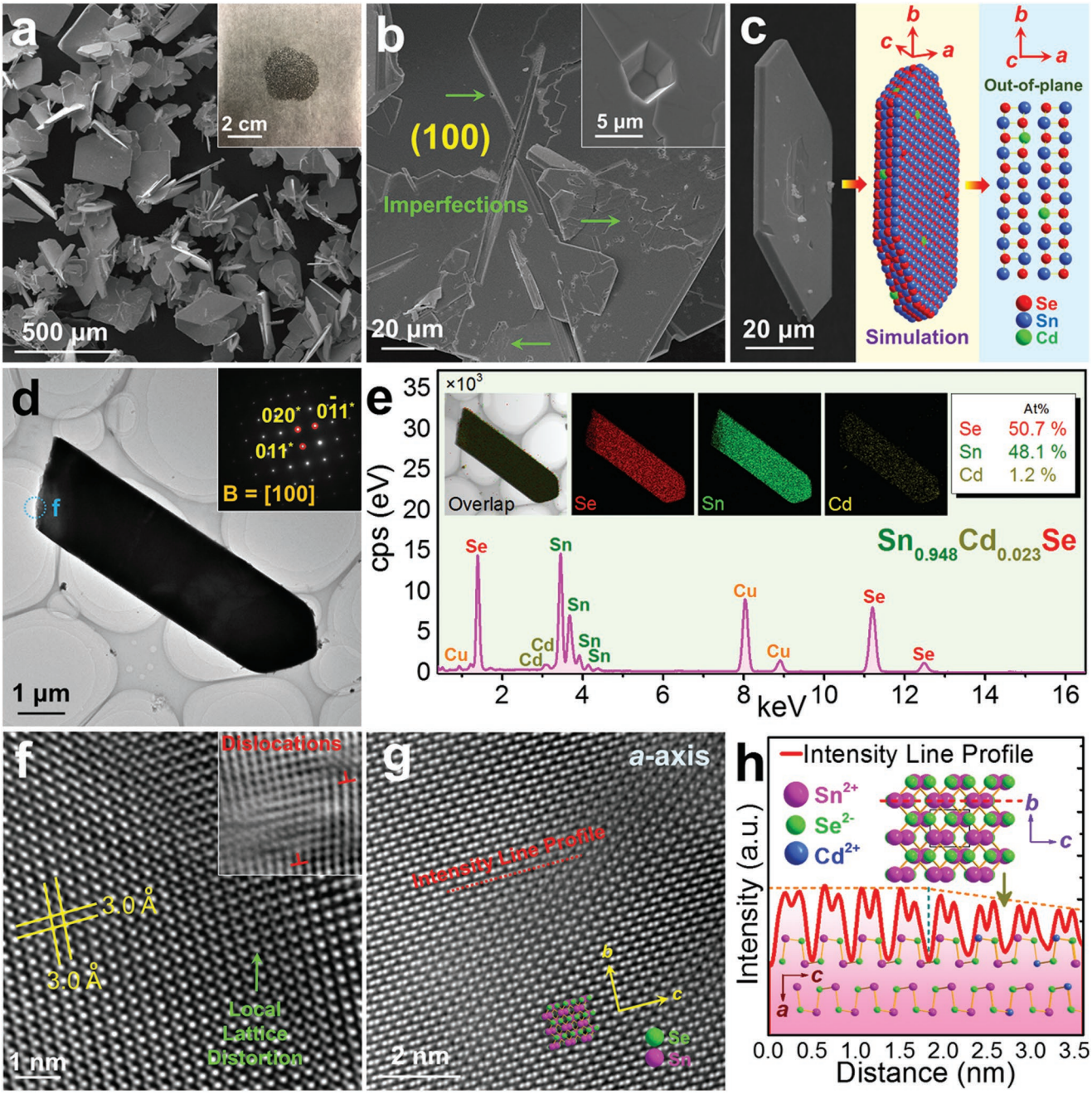

Figure 5. Morphological and compositional characterizations of the synthesized products. a) SEM image with inset of optical image of synthesized flower-like $Sn_{0.948}Cd_{0.023}Se$ microplates; b) magnified SEM image of one $Sn_{0.948}Cd_{0.023}Se$ microplate showing (100) surface with crystal imperfections exemplified in inset; c) one typical $Sn_{0.948}Cd_{0.023}Se$ microplate with simulated atomic model showing the out of plane; d) TEM image of a typical $Sn_{0.948}Cd_{0.023}Se$ microplate with inset of corresponding SAED pattern; e) EDS spot and mapping images. Cu comes from the TEM copper grid; f) HRTEM image circled in (d) to see the localized lattice distortion with inset of HRTEM image to see the dislocations; g) high-resolution Cs-STEM HAADF images to see the difference of contrast; h) corresponding intensity line profile taken from (g) to illustrate the potential reasons causing the contrast difference.

shows a [201] zone-axis HRTEM image, in which local lattice distortion is seen. Such local structural variations have been predicted to enhance the phonon scattering and in turn reduce κ_l.[3,21,23] Figure 7g shows STEM HAADF images taken from pure SnSe (left) and $Sn_{0.948}Cd_{0.023}Se$ (right) pellets, respectively, both viewed along their *b*-axes. As can be seen, $Sn_{0.948}Cd_{0.023}Se$ pellets contain nanoscale dark domains, similar to the reported "vacancy domains" caused by Sn vacancies.[32,49,50] Figure 7h is an enlarged STEM HAADF image taken from a typical boundary between normal and dark areas, in which the overlays in a normal area show axes and Se atoms in green and Sn atoms in purple. It is clear that a nonuniform contrast can

© 2019 WILEY-VCH Verlag GmbH & Co. KGaA, Weinheim

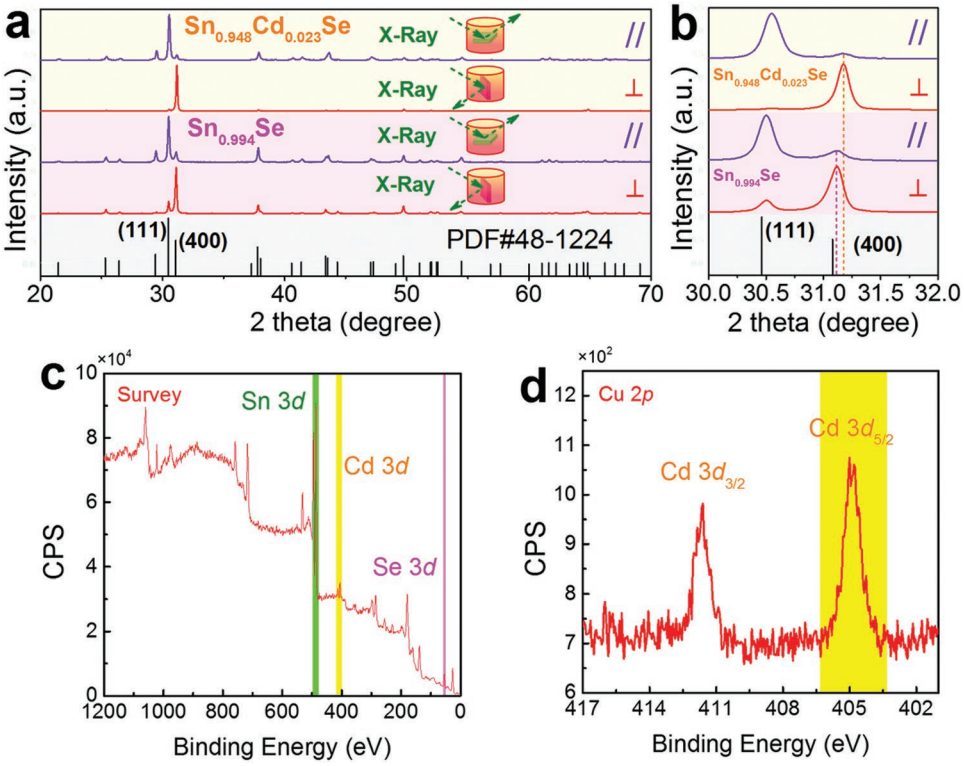

Figure 6. Structural and compositional characterizations of sintered pellets. a) XRD results of sintered $Sn_{0.994}Se$ and $Sn_{0.948}Cd_{0.023}Se$ pellets measured along different directions; b) magnified XRD results to see the deviations of 400* and 111* peak. XPS spectrum of c) survey scan for $Sn_{0.948}Cd_{0.023}Se$ pellet and d) high-resolution scan for Cd 3d.

be seen, suggesting local elemental variation. Besides, no interstitial atom can be found, indicating that there is no interstitial atom of Cd in the matrix of SnSe, supporting to the XPS results. Figure 7i is the intensity line profile (dashed purple line in Figure 7h across both normal area and contrast area) taken along the *c*-axis, from which the peak intensities for Se sites keep stable for the entire range, but different peak intensities for Sn sites between normal and dark areas, indicating local elemental variation such as Cd replacing Sn and/or cation vacancies, which can effectively scatter the high-frequency phonons and in turn contribute to a low κ_l.[3,21,23]

We measured σ, S, $S^2\sigma$, and κ as the main thermoelectric properties from 300 to 873 K for the Cd-doped SnSe pellets with different doping levels and the results are shown in **Figure 8**a–d, respectively. High repeatability was realized with measured fluctuations being 10%, 2%, and 5% for σ, S, and κ, respectively, as shown in Figure S6 in the Supporting Information. Besides, considering the anisotropy shown in Figure S7 in the Supporting Information,[7,14] the ⊥ direction is chosen as the main direction for measurements.[51] Figure 8a shows T-dependent σ. After Cd-doping, σ was significantly improved due to the improved cation vacancy concentration. As can be seen, the totality of σ values includes two regions. Taking $Sn_{0.948}Cd_{0.023}Se$ as an example, a representative metallic transport behavior can be seen before 723 K, derived from the vibration of cations, which can effectively impede the transport of carriers.[14] After 723 K, a classic thermally activated semiconducting behavior is observed, derived from the carrier thermal excitation by heat, which can produce extra carriers and improve the carrier concentration. The temperature between these two regions (723 K in the case of $Sn_{0.948}Cd_{0.023}Se$) is described as bipolar-effect temperature (T^*), where T^* increases from 623 to 723 K with increasing the doping level (cation vacancy concentration), fitting well with the reported calculation-based works.[3] Figure 8b shows the measured T-dependent S, in which peak S values can be achieved at T^*. With increasing the Cd-doping level, S gradually decreased, accompanied by a slight shifting of T^* toward a higher T, indicating an increase of p.[3,7] Figure 8c shows the determined $S^2\sigma$, from which two peak values of 7.33 μW cm^{-1} K^{-2} at 423 K and 6.86 μW cm^{-1} K^{-2} at 823 K can be found in the $Sn_{0.948}Cd_{0.023}Se$ pellet. Figure 8d shows the calculated T-dependent κ via $\kappa = D \cdot C_p \cdot \rho$,[7] where measured D values are plotted in Figure S8a in the Supporting Information, and measured C_p and ρ are listed in **Table 2**. As can be seen, with an increasing Cd-doping level, κ decreases, derived from the enhanced nanoscale crystal imperfections including locally distorted lattice, dislocations, and point defects. These nanoscale defects can effectively strengthen the scattering of phonons from medium and short wavelengths. Considering the high relative densities in our sintered pellets (all >97.1%),[14,19] the κ values are intrinsic.

To better understand our achieved electrical transport properties, we measured the T-dependent p. The result is shown in **Figure 9**a. A slightly increased p after T^* can be seen, triggered by thermal activation.[3] By increasing the Cd-doping level, p is improved, caused by the higher cation vacancy concentration.

© 2019 WILEY-VCH Verlag GmbH & Co. KGaA, Weinheim

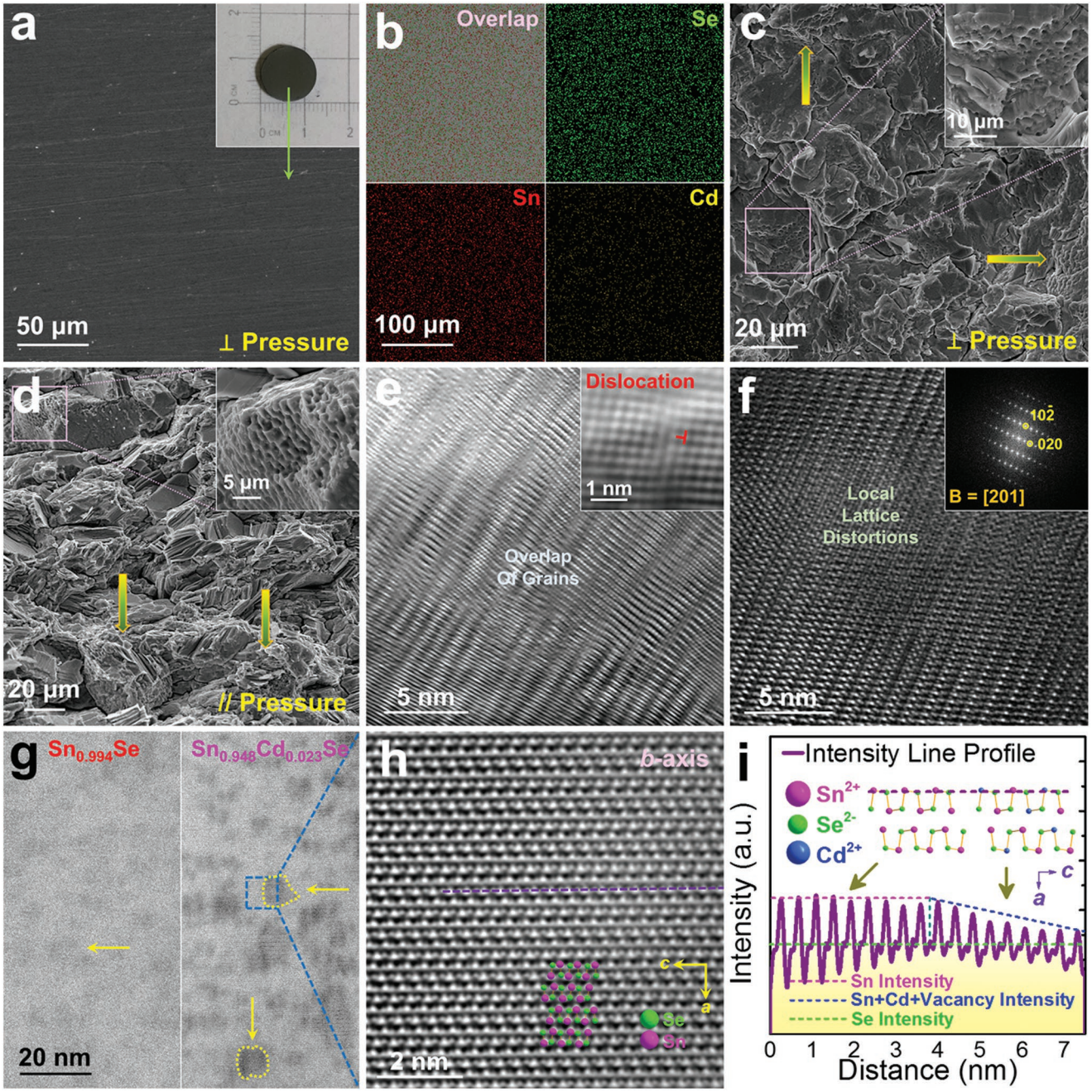

Figure 7. Morphological and compositional characterizations of sintered pellets. a) SEM image with inset of optical image of $Sn_{0.948}Cd_{0.023}Se$ pellet polished from the ⊥ direction; b) corresponding EDS mapping results for (a); SEM images of $Sn_{0.948}Cd_{0.023}Se$ pellet fractured from c) the ⊥ direction and d) the // direction, the inset magnified SEM images show the honeycomb-like structure; e) TEM image of sliced $Sn_{0.948}Cd_{0.023}Se$ pellet to see the overlap of grains with inset HRTEM image showing a typical dislocation; f) HRTEM image to show the local lattice distortion; g) Comparison of Cs-STEM HAADF images between $Sn_{0.994}Se$ (left) and $Sn_{0.948}Cd_{0.023}Se$ (right) pellets to see the difference; h) high-resolution Cs-STEM HAADF image of $Sn_{0.948}Cd_{0.023}Se$ pellet viewed along the *b*-axis to see different contrast; and i) corresponding intensity line profile taken from (h) to illustrate the potential reasons causing the contrast difference.

Figure 9b shows the corresponding T-dependent carrier mobility μ, which roughly follows the power law ($\mu \propto T^{d}$).[25,52] At low temperatures, μ is slightly increased, roughly following $\mu \propto T^{1.1}$, suggesting that the ionized impurities dominate the scattering mechanism.[25,52] At medium temperatures, μ is decreased following $\mu \propto T^{-1.5}$, meaning that acoustic-phonon scattering dominates the scattering mechanism instead.[25,52] At high temperatures, μ increases roughly following $\mu \propto T^{1.5}$, indicating extra scattering behaviors. Potential carrier scattering at local crystal imperfections observed in the Cd-doped SnSe may cause a special $\mu \propto T^{d}$ relation.[25,53,54] Besides, μ decreases with increasing Cd-doping level, which is caused

© 2019 WILEY-VCH Verlag GmbH & Co. KGaA, Weinheim

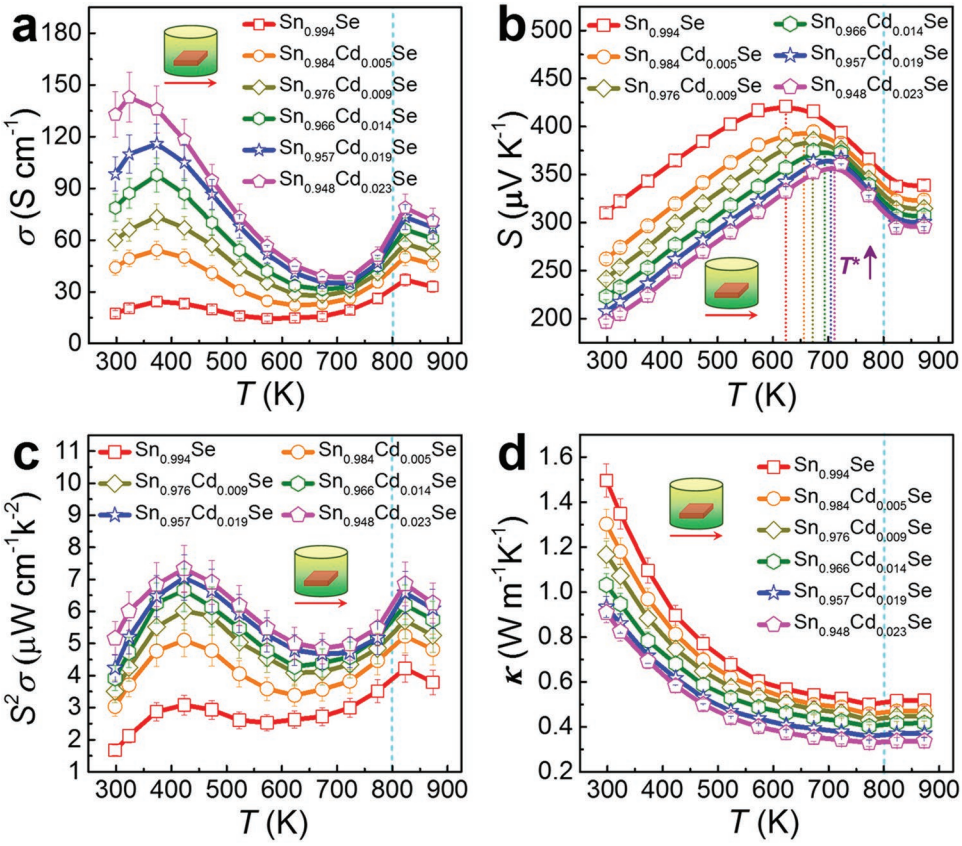

Figure 8. Plots of measured T-dependent properties from Cd-doped SnSe pellets: a) σ; b) S; c) $S^2\sigma$; and d) κ.

by the significant blocking and/or scattering of carriers. At high temperature, because the thermal activation can provide additional carriers (mainly holes as majority carriers),[3] with increasing doping level (cation vacancy concentration), additional carriers can be released, resulting in a lower μ between 600 and 800 K.

Table 2. The main properties of Cd-doped SnSe at both 300 and 823 K.

Parameters	$Sn_{0.994}Se$	$Sn_{0.984}Cd_{0.005}Se$	$Sn_{0.976}Cd_{0.009}Se$	$Sn_{0.966}Cd_{0.014}Se$	$Sn_{0.957}Cd_{0.019}Se$	$Sn_{0.948}Cd_{0.023}Se$
ρ (g cm^{-3})	6.121	6.103	6.077	6.045	6.021	6.002
$p_{300\ K}$ (cm^{-3})	2.79×10^{18}	7.29×10^{18}	9.98×10^{18}	1.33×10^{19}	1.71×10^{19}	2.33×10^{19}
$p_{823\ K}$ (cm^{-3})	7.71×10^{18}	1.17×10^{19}	1.48×10^{19}	1.91×10^{19}	2.25×10^{19}	2.60×10^{19}
$\mu_{300\ K}$ (cm^2 V^{-1} s^{-1})	39.0	37.8	37.6	37.0	35.9	35.5
$\mu_{823\ K}$ (cm^2 V^{-1} s^{-1})	29.9	26.8	24.4	21.7	20.4	18.9
$\sigma_{300\ K}$ (S cm^{-1})	17.4	44.2	60.1	78.8	98.3	132.9
$\sigma_{823\ K}$ (S cm^{-1})	37.0	50.3	58.0	62.2	73.4	78.8
$S_{300\ K}$ (μV K^{-1})	310.0	262.2	241.6	223.0	207.5	197.1
$S_{823\ K}$ (μV K^{-1})	337.9	322.5	313.8	306.2	299.5	295.1
$S^2\sigma_{300\ K}$ (μW cm^{-1} K^{-2})	1.67	3.04	3.51	3.92	4.23	5.16
$S^2\sigma_{823\ K}$ (μW cm^{-1} K^{-2})	4.22	5.23	5.71	6.20	6.58	6.86
$C_{p300\ K}$ (J g^{-1} K^{-1})	0.273	0.27	0.267	0.263	0.259	0.254
$C_{p823\ K}$ (J g^{-1} K^{-1})	0.286	0.281	0.277	0.272	0.268	0.264
$\kappa_{300\ K}$ (W m^{-1} K^{-1})	1.50	1.30	1.17	1.03	0.93	0.91
$\kappa_{823\ K}$ (W m^{-1} K^{-1})	0.52	0.47	0.45	0.42	0.37	0.33

© 2019 WILEY-VCH Verlag GmbH & Co. KGaA, Weinheim

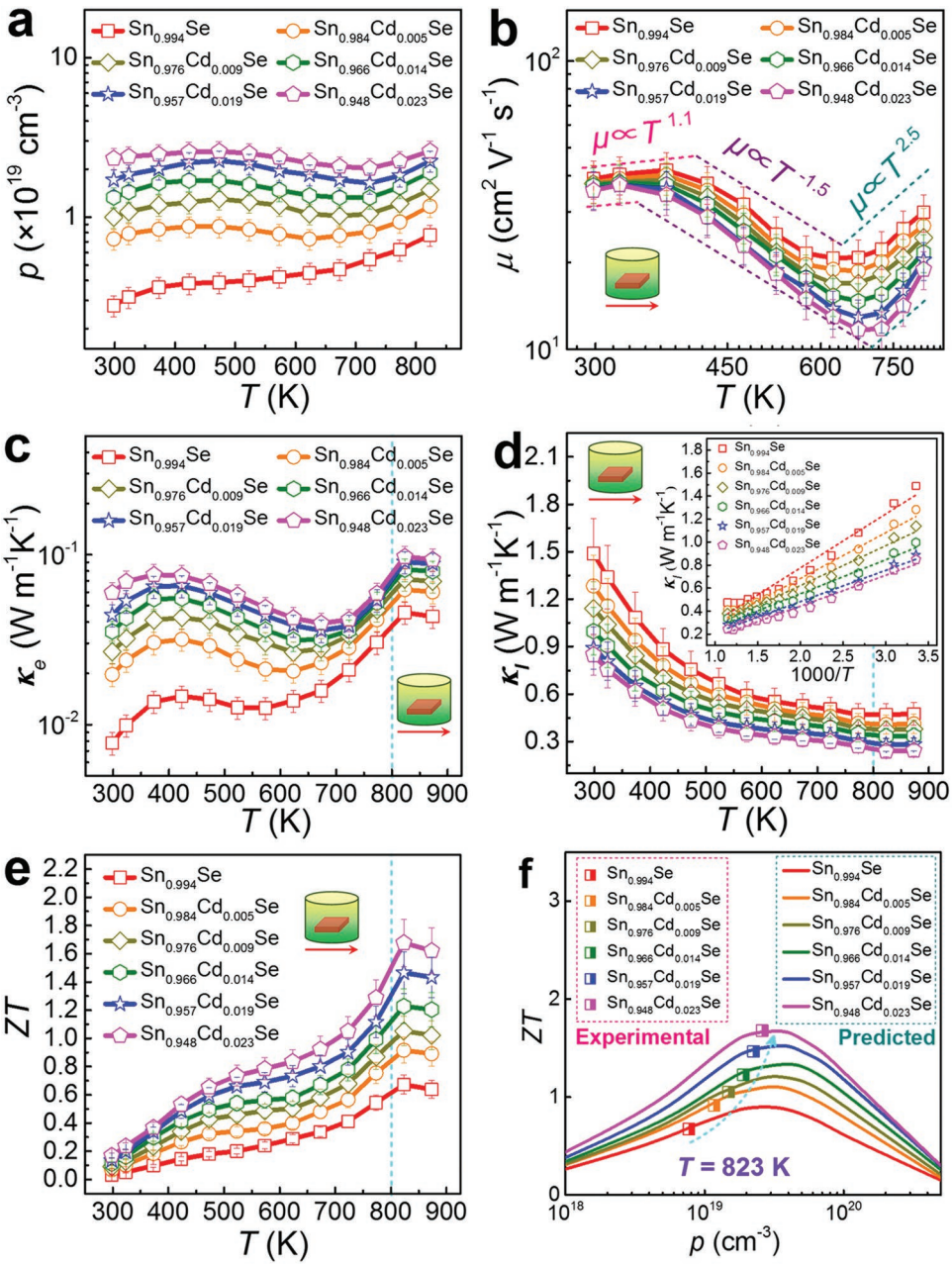

Figure 9. Plots of measured and/or calculated *T*-dependent properties for Cd-doped SnSe pellets: a) p; b) μ; c) κ_e; d) κ_l with 1000/*T*-dependent κ_l as inset; and e) *ZT*. f) A comparison of achieved *ZT*s with calculated predicted *ZT*s.

To further understand the electronic structure and DOS evolution of the Cd-doped SnSe with different cation vacancy concentrations, we performed DFT calculations. **Figure 10**a–c compares the calculated band structures for $Sn_{0.994}Se$, $Sn_{0.976}Cd_{0.009}Se$, and $Sn_{0.957}Cd_{0.019}Se$, respectively, and Figure 10d compares the DOS of $Sn_{0.994}Se$, $Sn_{0.984}Cd_{0.005}Se$, $Sn_{0.976}Cd_{0.009}Se$, $Sn_{0.966}Cd_{0.014}Se$, $Sn_{0.957}Cd_{0.019}Se$, and $Sn_{0.948}Cd_{0.023}Se$, respectively. It is clear that the Fermi level moves toward the valence band with increasing cation vacancy concentration, indicating a degenerate semiconductor which can provide more holes, contributing to an improved p and in turn an enhanced $S^2\sigma$, agreeing with the experimental results shown in Figure 9.

For the thermal transport performance, κ_e and κ_l are investigated to further understand the contributions of electrons and lattice on the total thermal conductivity κ. κ_e is obtained via $\kappa_e = L\cdot\sigma\cdot T$ by the Wiedemann–Franz law.[3] Here L is the Lorenz number ($\approx 1.5 \times 10^{-8}$ V^2 K^{-2}) calculated via the SPB model[42–44] as shown in Figure S8c in the Supporting Information, and κ_l is determined by $\kappa_l = \kappa - \kappa_e$. Figure 9c shows the determined κ_e with very low values, which have the same trend compared with the corresponding σ. Figure 9d shows

© 2019 WILEY-VCH Verlag GmbH & Co. KGaA, Weinheim

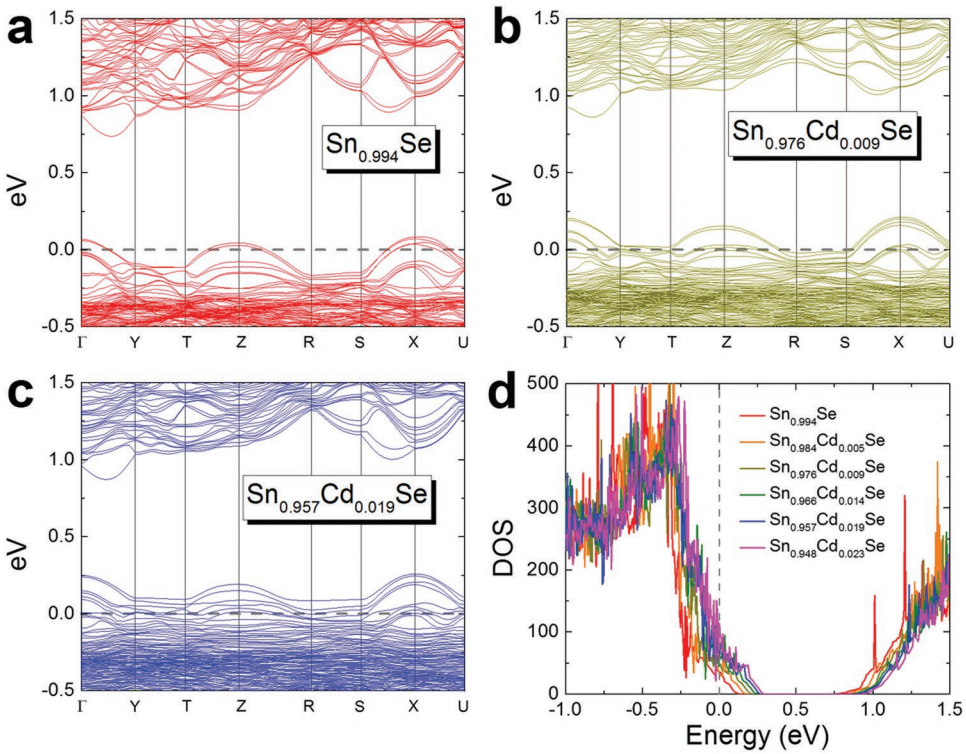

Figure 10. Comparisons of calculated band structures for a) $Sn_{0.994}Se$, b) $Sn_{0.976}Cd_{0.009}Se$, and c) $Sn_{0.957}Cd_{0.019}Se$; and d) comparisons of DOS of $Sn_{0.994}Se$, $Sn_{0.984}Cd_{0.005}Se$, $Sn_{0.976}Cd_{0.009}Se$, $Sn_{0.966}Cd_{0.014}Se$, $Sn_{0.957}Cd_{0.019}Se$, and $Sn_{0.948}Cd_{0.023}Se$.

the determined T-dependent κ_l, with the inset showing the determined $1000/T$-dependent κ_l roughly following a linear relationship, showing that Umklapp phonon scattering dominates phonon scattering in SnSe.[26,55] Such intrinsic low κ_l have been derived from significantly anharmonic bonding[3,7,14,21,23,26] and the observed nanoscale crystal imperfections including the dislocations, local lattice distortions, point defects (vacancy domains), grain boundaries, and/or interfaces, which can effectively scatter phonons of different wavelengths.[1,3] The calculated κ_l/κ ratio of $\gtrsim$70% (refer to Figure S8d in the Supporting Information), indicates that phonon transport is significant for κ.

Figure 9e presents the calculated T-dependent ZT values for the Cd-doped SnSe pellets, indicating that the improved cation vacancy concentration is critical for securing a high ZT value. The high ZTs (>0.6) are in a wide range from 450 to 873 K, which is of significance because the device has to be operated under a large temperature gradient.[1,3] Figure 9f compares the achieved ZT values with predicted values determined by the SPB model-based calculations at 823 K.[42–45] As can be seen, the measured $p = \approx 2.6 \times 10^{19}$ cm^{-3} is much closer to the best value of $\approx 3 \times 10^{19}$ cm^{-3} as we calculated, indicating that p can be indeed tuned through our developed methodology. **Table 3** compares our achieved thermoelectric properties with reported studies, showing a strong competitiveness in our polycrystalline Cd-doped SnSe fabricated via a facile solvothermal synthesis. It should be mentioned that SnSe is a typical low-toxic and high cost-effective thermoelectric material.[3,51] Even though Cd is a toxic element,[56] the amount of Cd in our SnSe system is very low (only ≈2.3%), thus our Cd-doped SnSe is still a green thermoelectric material.

3. Conclusion

In this study, a combination of cation vacancy engineering and local lattice engineering is used to realize excellent thermoelectric properties in p-type polycrystalline Cd-doped SnSe via a facile solvothermal synthesis method and a fast spark plasma sintering technique. The Cd solubility in SnSe is ≈2.3 at% with a high cation vacancy concentration of ≈2.9%, contributing to a high hole carrier concentration of $\approx 2.6 \times 10^{19}$ cm^{-3} and in turn leading to a high power factor of ≈6.9 μW cm^{-1} K^{-2} at 823 K. Meanwhile, the doped Cd results in massive nanoscale crystal imperfections including dislocations, intensive local lattice distortions, and point defects, which contribute to a low thermal conductivity of ≈0.33 W m^{-1} K^{-1} and in turn a record high ZT of ≈1.7 at this temperature. This study explores the fundamental Cd-doping mechanisms at a nanoscale in a SnSe matrix and describes a novel concept to achieve high ZT.

4. Experimental Section

The experimental details can be seen in Section S9 in the Supporting Information.

© 2019 WILEY-VCH Verlag GmbH & Co. KGaA, Weinheim

Table 3. A comparison of performance from p-type doped polycrystalline SnSe. Here, ST, HT, M, ZM, A, SSR, MA, and HP mean solvothermal, hydrothermal, melting, zone-melting, annealing, solid-state solution, mechanical alloying, and hot-pressing, respectively.

Product	Synthetic method	ZT	T [K]	σ [S cm^{-1}]	S [μV K^{-1}]	$S^2\sigma$ [mW m^{-1} K^{-2}]	K [W m^{-1} K^{-1}]	p [10^{19} cm^{-3}]	ρ [g cm^{-3}]	Ref.
$Sn_{0.948}Cd_{0.023}Se$	ST+SPS	1.7	823	≈78.8	≈295.1	≈0.69	≈0.33	≈2.60	≈6.00	This work
$Sn_{0.99}Na_{0.01}Se$	M+SPS	0.75	823	≈49.6	≈311.1	0.48	≈0.53	1.0[a)]	≈5.99	[57]
$Sn_{0.99}Na_{0.01}Se$	M+SPS	≈0.8	800	≈81.2	≈267.2	≈0.58	≈0.50	≈1.5	–	[12]
$Sn_{0.99}Na_{0.01}Se$	M+A+SPS	0.85	800	≈100.4	≈271.5	≈0.74	≈0.50	≈6.5[a)]	5.94	[58]
$Sn_{0.985}Na_{0.015}Se$	M+MA+HP	≈0.8	773	≈37.9	≈298.8	≈0.34	≈0.33	≈2.1[a)]	5.81	[59]
$Sn_{0.98}Na_{0.02}Se$	SPS	0.87	798	≈56.4	≈288.8	0.47	0.4	3.08[a)]	≈5.81	[60]
$Sn_{0.97}Na_{0.03}Se$	SPS	0.82	773	≈65.1	≈280.2	≈0.51	≈0.50	≈2.2	≈5.93	[61]
$Sn_{0.99}Na_{0.005}K_{0.005}Se$	MA+SPS	1.2	773	≈34.9	≈374.7	≈0.49	0.32	≈7.2[a)]	5.71	[37]
$Sn_{0.995}Na_{0.005}SeCl_{0.005}$	SSR+HP	0.84	810	≈79.2	≈228.6	≈0.41	≈0.39	≈3.95[a)]	≈5.93	[62]
$Sn_{0.99}Na_{0.01}Se_{0.84}Te_{0.16}$	MA+SPS	0.72	773	≈67.4	≈275.0	≈0.51	≈0.50	–	–	[13]
$(Sn_{0.96}Pb_{0.04})_{0.99}Na_{0.01}Se$	M+SPS	≈1.2	773	≈89.4	≈269.7	≈0.65	≈0.45	≈2.8	–	[63]
$Sn_{0.99}K_{0.01}Se$	MA+SPS	≈1.1	773	≈18.6	≈421.4	≈0.33	≈0.24	0.92[a)]	–	[64]
$SnSe_{0.985}Cl_{0.015}$	M	1.1	773	≈25.5	≈399.3	≈0.41	≈0.30	≈0.01[a)]	5.87	[36]
$Sn_{0.99}Zn_{0.01}Se$	M+HP	0.96	873	≈74.1	≈328.5	0.8	≈0.73	≈0.45	–	[40]
$Sn_{0.9}Ge_{0.1}Se$	M	–	400	–	≈843.2	–	≈0.39	–	–	[65]
$Sn_{0.96}Ge_{0.04}Se$	ZM+HP	0.6	823	35.6	≈378.5	0.51	≈0.7	≈0.03[a)]	>5.81	[39]
$Sn_{0.99}Cu_{0.01}Se$	HT+HP	1.2	873	≈36.4	≈313.8	≈0.35	≈0.2	–	–	[66]
$Sn_{0.98}Cu_{0.02}Se$	M+A+SPS	0.7	773	≈42.4	≈238.6	≈0.24	0.27	18.4[a)]	≈6.12	[67]
$Sn_{0.97}Cu_{0.03}Se$	M+HP	0.79	823	≈35.0	≈325.1	≈0.37	≈0.39	≈0.016[a)]	6.16	[68]
$Sn_{0.99}Ag_{0.01}Se$	M+A+HP	0.6	750	≈45.9	≈344.1	≈0.54	≈0.68	≈0.35[a)]	≈5.93	[69]
$Sn_{0.99}Ag_{0.01}Se$	M+A+SPS	0.74	823	≈54.8	≈330.9	0.6	≈0.66	1.9[a)]	≈5.99	[70]
$Sn_{0.985}Ag_{0.015}Se$	M	1.3	773	≈44.7	≈344.0	≈0.52	≈0.30	≈0.8[a)]	5.87	[36]
$Sn_{0.97}Ag_{0.03}Se$	ST+SPS	0.8	850	≈90.3	≈266.2	≈0.64	≈0.68	0.9[a)]	>5.56	[71]
$Sn_{0.995}Tl_{0.005}Se$	M+HP	0.6	725	≈68.9	≈300.0	≈0.62	≈0.75	–	≈5.99	[72]
$Sn_{0.99}In_{0.01}Se$	M+HP	0.2	823	≈6.53	≈350.0	≈0.08	≈0.36	≈0.03[a)]	≈5.87	[73]
$Sn_{0.97}Sm_{0.03}Se$	M+HP	0.55	823	≈33.6	≈250.0	≈0.21	≈0.32	≈0.013[a)]	–	[47]
$SnSe_{0.9}Te_{0.1}$	ST+SPS	1.1	800	≈57.4	≈322.8	≈0.60	≈0.44	≈1[a)]	≈5.87	[38]

[a)]The room temperature-measured p.

Supporting Information

Supporting Information is available from the Wiley Online Library or from the author.

Acknowledgements

X.-L.S. and A.-Y.W. contributed equally to this work. This work was financially supported by the Australian Research Council and the National Natural Science Foundation of China (11774016). X.-L.S thanks the IPRS for providing his PhD program. The Australian Microscopy & Microanalysis Research Facility is acknowledged for providing characterization facilities. Theoretical work by T.F. and S.T.P. was supported in part by Department of Energy grant DE-FG0209ER46554 and by the McMinn Endowment. Computations at Vanderbilt University and ORNL were performed at the National Energy Research Scientific Computing Center (NERSC), a Department of Energy, Office of Science, User Facility funded through Contract No. DE-AC02-05CH11231. Computations also used the Extreme Science and Engineering Discovery Environment (XSEDE).

Conflict of Interest

The authors declare no conflict of interest.

Keywords

Cd-doping, characterization, solvothermal, thermoelectric, tin selenide

Received: October 18, 2018
Revised: January 7, 2019
Published online:

[1] T. Zhu, Y. Liu, C. Fu, J. P. Heremans, J. G. Snyder, X. Zhao, *Adv. Mater.* **2017**, *29*, 1605884.
[2] L.-D. Zhao, V. P. Dravid, M. G. Kanatzidis, *Energy Environ. Sci.* **2014**, *7*, 251.
[3] Z.-G. Chen, X. Shi, L.-D. Zhao, J. Zou, *Prog. Mater. Sci.* **2018**, *97*, 283.

 © 2019 WILEY-VCH Verlag GmbH & Co. KGaA, Weinheim

[4] R. Moshwan, L. Yang, J. Zou, Z.-G. Chen, *Adv. Funct. Mater.* **2017**, *27*, 1703278.
[5] K. Zhao, H. Duan, N. Raghavendra, P. Qiu, Y. Zeng, W. Zhang, J. Yang, X. Shi, L. Chen, *Adv. Mater.* **2017**, *29*, 1701148.
[6] M. S. Dresselhaus, G. Chen, M. Y. Tang, R. G. Yang, H. Lee, D. Z. Wang, Z. F. Ren, J. P. Fleurial, P. Gogna, *Adv. Mater.* **2007**, *19*, 1043.
[7] X. Shi, Z. Chen, W. Liu, L. Yang, M. Hong, R. Moshwan, L. Huang, J. Zou, *Energy Storage Mater.* **2018**, *10*, 130.
[8] W. D. Liu, Z. G. Chen, J. Zou, *Adv. Energy Mater.* **2018**, *8*, 1800056.
[9] K. Kutorasinski, B. Wiendlocha, S. Kaprzyk, J. Tobola, *Phys. Rev. B* **2015**, *91*, 205201.
[10] Y. Zhou, L.-D. Zhao, *Adv. Mater.* **2017**, *29*, 1702676.
[11] T.-R. Wei, C.-F. Wu, F. Li, J.-F. Li, *J. Materiomics* **2018**, *4*, 304.
[12] T. R. Wei, G. Tan, X. Zhang, C. F. Wu, J. F. Li, V. P. Dravid, G. J. Snyder, M. G. Kanatzidis, *J. Am. Chem. Soc.* **2016**, *138*, 8875.
[13] T. R. Wei, C. F. Wu, X. Zhang, Q. Tan, L. Sun, Y. Pan, J. F. Li, *Phys. Chem. Chem. Phys.* **2015**, *17*, 30102.
[14] L. D. Zhao, S. H. Lo, Y. Zhang, H. Sun, G. Tan, C. Uher, C. Wolverton, V. P. Dravid, M. G. Kanatzidis, *Nature* **2014**, *508*, 373.
[15] C. Chang, M. Wu, D. He, Y. Pei, C.-F. Wu, X. Wu, H. Yu, F. Zhu, K. Wang, Y. Chen, *Science* **2018**, *360*, 778.
[16] L.-D. Zhao, C. Chang, G. Tan, M. G. Kanatzidis, *Energy Environ. Sci.* **2016**, *9*, 3044.
[17] S. Sassi, C. Candolfi, J. B. Vaney, V. Ohorodniichuk, P. Masschelein, A. Dauscher, B. Lenoir, *Appl. Phys. Lett.* **2014**, *104*, 212105.
[18] L.-D. Zhao, G. Tan, S. Hao, J. He, Y. Pei, H. Chi, H. Wang, S. Gong, H. Xu, V. P. Dravid, *Science* **2016**, *351*, 141.
[19] P.-C. Wei, S. Bhattacharya, J. He, S. Neeleshwar, R. Podila, Y. Chen, A. Rao, *Nature* **2016**, *539*, E1.
[20] D. Ibrahim, J.-B. Vaney, S. Sassi, C. Candolfi, V. Ohorodniichuk, P. Levinsky, C. Semprimoschnig, A. Dauscher, B. Lenoir, *Appl. Phys. Lett.* **2017**, *110*, 032103.
[21] X. L. Shi, K. Zheng, W. D. Liu, Y. Wang, Y. Z. Yang, Z. G. Chen, J. Zou, *Adv. Energy Mater.* **2018**, *8*, 1800775.
[22] C. Chang, Q. Tan, Y. Pei, Y. Xiao, X. Zhang, Y.-X. Chen, L. Zheng, S. Gong, J.-F. Li, J. He, *RSC Adv.* **2016**, *6*, 98216.
[23] X. L. Shi, K. Zheng, M. Hong, W. D. Liu, R. Moshwan, Y. Wang, X.-L. Qu, Z. G. Chen, J. Zou, *Chem. Sci.* **2018**, *9*, 7376.
[24] Y.-M. Han, J. Zhao, M. Zhou, X.-X. Jiang, H.-Q. Leng, L.-F. Li, *J. Mater. Chem. A* **2015**, *3*, 4555.
[25] Y. Li, F. Li, J. Dong, Z. Ge, F. Kang, J. He, H. Du, B. Li, J.-F. Li, *J. Mater. Chem. C* **2016**, *4*, 2047.
[26] K. Peng, X. Lu, H. Zhan, S. Hui, X. Tang, G. Wang, J. Dai, C. Uher, G. Wang, X. Zhou, *Energy Environ. Sci.* **2016**, *9*, 454.
[27] A. T. Duong, V. Q. Nguyen, G. Duvjir, V. T. Duong, S. Kwon, J. Y. Song, J. K. Lee, J. E. Lee, S. Park, T. Min, J. Lee, J. Kim, *Nat. Commun.* **2016**, *7*, 13713.
[28] L. Yang, Z.-G. Chen, M. S. Dargusch, J. Zou, *Adv. Energy Mater.* **2018**, *8*, 1701797.
[29] B. Li, Y. Xie, J. Huang, Y. Qian, *Inorg. Chem.* **2000**, *39*, 2061.
[30] J. Dai, J. Sun, A. Xie, J. He, C. Li, Y. Yan, *RSC Adv.* **2016**, *6*, 3446.
[31] T. Schröder, T. Rosenthal, N. Giesbrecht, M. Nentwig, S. Maier, H. Wang, G. J. Snyder, O. Oeckler, *Inorg. Chem.* **2014**, *53*, 7722.
[32] W. Wei, C. Chang, T. Yang, J. Liu, H. Tang, J. Zhang, Y. Li, F. Xu, Z. Zhang, J.-F. Li, *J. Am. Chem. Soc.* **2018**, *140*, 499.
[33] N. V. Quang, D. A. Tuan, D. V. Thiet, N. T. Minh Hai, G. Duvjir, T. T. Ly, K. Jungdae, C. Sunglae, *Bull. Am. Phys. Soc.* **2017**, *62*, 4.
[34] Q. Li, L. Zhang, J. Yin, Z. Sheng, X. Chu, F. Wang, F. Zhu, *J. Alloys Compd.* **2018**, *745*, 513.
[35] A. Takeuchi, A. Inoue, *Mater. Trans.* **2005**, *46*, 2817.
[36] L. Zhang, J. Wang, Q. Sun, P. Qin, Z. Cheng, Z. Ge, Z. Li, S. Dou, *Adv. Energy Mater.* **2017**, *7*, 1700573.
[37] Z.-H. Ge, D. Song, X. Chong, F. Zheng, L. Jin, X. Qian, L. Zheng, R. E. Dunin-Borkowski, P. Qin, J. Feng, *J. Am. Chem. Soc.* **2017**, *139*, 9714.
[38] M. Hong, Z.-G. Chen, L. Yang, T. C. Chasapis, S. D. Kang, Y. Zou, G. J. Auchterlonie, M. G. Kanatzidis, G. J. Snyder, J. Zou, *J. Mater. Chem. A* **2017**, *5*, 10713.
[39] Y. Fu, J. Xu, G.-Q. Liu, X. Tan, Z. Liu, X. Wang, H. Shao, H. Jiang, B. Liang, J. Jiang, *J. Electron. Mater.* **2017**, *46*, 3182.
[40] J. C. Li, D. Li, X. Y. Qin, J. Zhang, *Scr. Mater.* **2017**, *126*, 6.
[41] G. Tang, W. Wei, J. Zhang, Y. Li, X. Wang, G. Xu, C. Chang, Z. Wang, Y. Du, L.-D. Zhao, *J. Am. Chem. Soc.* **2016**, *138*, 13647.
[42] Y. Xu, W. Li, C. Wang, J. Li, Z. Chen, S. Lin, Y. Chen, Y. Pei, *J. Mater. Chem. A* **2017**, *5*, 19143.
[43] J. Shen, Z. Chen, S. lin, L. Zheng, W. Li, Y. Pei, *J. Mater. Chem. C* **2016**, *4*, 209.
[44] X. She, X. Su, H. Du, T. Liang, G. Zheng, Y. Yan, R. Akram, C. Uher, X. Tang, *J. Mater. Chem. C* **2015**, *3*, 12116.
[45] L. Zhao, S. M. K. N. Islam, J. Wang, D. L. Cortie, X. Wang, Z. Cheng, J. Wang, N. Ye, S. Dou, X. Shi, L. Chen, G. J. Snyder, X. Wang, *Nano Energy* **2017**, *41*, 164.
[46] D. G. Cahill, S. K. Watson, R. O. Pohl, *Phys. Rev. B* **1992**, *46*, 6131.
[47] J. Gao, H. Zhu, T. Mao, L. Zhang, J. Di, G. Xu, *Mater. Res. Bull.* **2017**, *93*, 366.
[48] J. Yang, L. Fei, H. Liu, Y. Liu, M. Gao, Y. Zhang, L. Yang, *J. Alloys Compd.* **2011**, *509*, 3672.
[49] S. Hillyard, J. Silcox, *Ultramicroscopy* **1995**, *58*, 6.
[50] P. Nellist, S. Pennycook, *Ultramicroscopy* **1999**, *78*, 111.
[51] X. Shi, A. Wu, W. Liu, R. Moshwan, Y. Wang, Z.-G. Chen, J. Zou, *ACS Nano* **2018**, *12*, 11417.
[52] M. Nassary, *Turk. J. Phys.* **2009**, *33*, 201.
[53] Q. Tan, L.-D. Zhao, J.-F. Li, C.-F. Wu, T.-R. Wei, Z.-B. Xing, M. G. Kanatzidis, *J. Mater. Chem. A* **2014**, *2*, 17302.
[54] J. Martin, L. Wang, L. Chen, G. Nolas, *Phys. Rev. B* **2009**, *79*, 115311.
[55] D. R. Clarke, *Surf. Coat. Technol.* **2003**, *163-164*, 67.
[56] P. Das, S. Samantaray, G. Rout, *Environ. Pollut.* **1997**, *98*, 29.
[57] H.-Q. Leng, M. Zhou, J. Zhao, Y.-M. Han, L.-F. Li, *RSC Adv.* **2016**, *6*, 9112.
[58] T.-R. Wei, G. Tan, C.-F. Wu, C. Chang, L.-D. Zhao, J.-F. Li, G. J. Snyder, M. G. Kanatzidis, *Appl. Phys. Lett.* **2017**, *110*, 053901.
[59] E. K. Chere, Q. Zhang, K. Dahal, F. Cao, J. Mao, Z. Ren, *J. Mater. Chem. A* **2016**, *4*, 1848.
[60] B. Cai, J. Li, H. Sun, P. Zhao, F. Yu, L. Zhang, D. Yu, Y. Tian, B. Xu, *J. Alloys Compd.* **2017**, *727*, 1014.
[61] K. Peng, H. Wu, Y. Yan, L. Guo, G. Wang, X. Lu, X. Zhou, *J. Mater. Chem. A* **2017**, *5*, 14053.
[62] S. D. Yang, R. K. Nutor, Z. J. Chen, H. Zheng, H. F. Wu, J. X. Si, *J. Electron. Mater.* **2017**, *46*, 6662.
[63] Y. K. Lee, K. Ahn, J. Cha, C. Zhou, H. S. Kim, G. Choi, S. I. Chae, J.-H. Park, S.-P. Cho, S. H. Park, Y.-E. Sung, W. B. Lee, T. Hyeon, I. Chung, *J. Am. Chem. Soc.* **2017**, *139*, 10887.
[64] Y.-X. Chen, Z.-H. Ge, M. Yin, D. Feng, X.-Q. Huang, W. Zhao, J. He, *Adv. Funct. Mater.* **2016**, *26*, 6836.
[65] M. Gharsallah, F. Serrano-Sanchez, N. M. Nemes, F. J. Mompean, J. L. Martinez, M. T. Fernandez-Diaz, F. Elhalouani, J. A. Alonso, *Sci. Rep.* **2016**, *6*, 26774.
[66] Y. Gong, C. Chang, W. Wei, J. Liu, W. Xiong, S. Chai, D. Li, J. Zhang, G. Tang, *Scr. Mater.* **2018**, *147*, 74.

© 2019 WILEY-VCH Verlag GmbH & Co. KGaA, Weinheim

[67] N. K. Singh, S. Bathula, B. Gahtori, K. Tyagi, D. Haranath, A. Dhar, *J. Alloys Compd.* **2016**, *668*, 152.
[68] J. Gao, G. Xu, *Intermetallics* **2017**, *89*, 40.
[69] C.-L. Chen, H. Wang, Y.-Y. Chen, T. Day, G. J. Snyder, *J. Mater. Chem. A* **2014**, *2*, 11171.
[70] H. Leng, M. Zhou, J. Zhao, Y. Han, L. Li, *J. Electron. Mater.* **2016**, *45*, 527.
[71] C.-H. Chien, C.-C. Chang, C.-L. Chen, C.-M. Tseng, Y.-R. Wu, M.-K. Wu, C.-H. Lee, Y.-Y. Chen, *RSC Adv.* **2017**, *7*, 34300.
[72] V. Kucek, T. Plechacek, P. Janicek, P. Ruleova, L. Benes, J. Navratil, C. Drasar, *J. Electron. Mater.* **2016**, *45*, 2943.
[73] J. H. Kim, S. Oh, Y. M. Kim, H. S. So, H. Lee, J.-S. Rhyee, S.-D. Park, S.-J. Kim, *J. Alloys Compd.* **2016**, *682*, 785.

© 2019 WILEY-VCH Verlag GmbH & Co. KGaA, Weinheim

Copyright WILEY-VCH Verlag GmbH & Co. KGaA, 69469 Weinheim, Germany, 2019.

ADVANCED ENERGY MATERIALS

Supporting Information

for *Adv. Energy Mater.*, DOI: 10.1002/aenm.201803242

High Thermoelectric Performance in p-type Polycrystalline Cd-doped SnSe Achieved by a Combination of Cation Vacancies and Localized Lattice Engineering

Xiaolei Shi, Angyin Wu, Tianli Feng, Kun Zheng, Weidi Liu, Qiang Sun, Min Hong, Sokrates T. Pantelides, Zhi-Gang Chen, and Jin Zou**

Supporting Information

High thermoelectric performance in *p*-type polycrystalline Cd-doped SnSe achieved by a combination of cation vacancies and localized lattice engineering

Xiaolei Shi, Angyin Wu, Tianli Feng, Kun Zheng, Weidi Liu, Qiang Sun, Min Hong, Sokrates T. Pantelides, Zhi-Gang Chen, and Jin Zou**

X-L. Shi, A-Y. Wu, W-D. Liu, Q. Sun, Prof. Z-G. Chen and Prof. J. Zou
Materials Engineering, the University of Queensland, Brisbane, QLD 4072, Australia
E-mail: zhigang.chen@uq.edu.au; j.zou@uq.edu.au
T. Feng, Prof. S. T. Pantelides
Department of Physics and Astronomy and Department of Electrical Engineering and Computer Science, Vanderbilt University, Nashville, Tennessee 37235, USA
Materials Science and Technology Division, Oak Ridge National Laboratory, Oak Ridge, Tennessee 37831, USA
Prof. K. Zheng
Beijing Key Lab of Microstructure and Property of Solids, Institute of Microstructure and Properties of Advanced Materials, Beijing University of Technology, Beijing 100124, China
M. Hong, Prof. Z-G Chen
Centre for Future Materials, University of Southern Queensland, Springfield, QLD 4300, Australia
E-mail: zhigang.chen@usq.edu.au;
Prof. J. Zou
Centre for Microscopy and Microanalysis, the University of Queensland, Brisbane, QLD 4072, Australia

Keywords: thermoelectric, solvothermal, tin selenide, Cd-doping, characterization.

Section 1. Calculation details for the prediction of *ZT* and the discussion for the effect of Cd-doping on the conduction band of SnSe.

The single parabolic band (SPB) model has been comprehensively used in predicting thermoelectric efficiencies (*ZT*) and optimizing doping levels (electronic or hole concentrations) for a number of thermoelectric materials.[1-4] In this study, we used SPB model to calculate the hole concentrations *p*-dependent *ZT* for polycrystalline SnSe at a fixed temperature of 873 K. The predicted *ZT* values in **Figure 9(f)** are also calculated based on this model at 823 K, and the κ_l used in the calculation are derived from **Figure 9(d)**. For calculation details, the carrier transport property analysis was employed as:

$$S(\eta) = \frac{k_B}{e} \cdot \left[\frac{\left(r+\frac{5}{2}\right) \cdot F_{r+\frac{3}{2}}(\eta)}{\left(r+\frac{3}{2}\right) \cdot F_{r+\frac{1}{2}}(\eta)} - \eta \right] \quad \text{(S1-1)}$$

$$p = \frac{1}{e \cdot R_H} = \frac{(2m^* \cdot k_B T)^{\frac{3}{2}}}{3\pi^2 \hbar^3} \cdot \frac{\left(r+\frac{3}{2}\right)^2 \cdot F^2_{r+\frac{1}{2}}(\eta)}{(2r+\frac{3}{2}) \cdot F_{2r+\frac{1}{2}}(\eta)} \quad \text{(S1-2)}$$

$$\mu = \left[\frac{e\pi\hbar^4}{\sqrt{2}(k_B T)^{\frac{3}{2}}} \frac{C_l}{{E_{def}}^2 (m^*)^{\frac{5}{2}}} \right] \frac{(2r+\frac{3}{2}) \cdot F_{2r+\frac{1}{2}}(\eta)}{\left(r+\frac{3}{2}\right)^2 \cdot F_{r+\frac{1}{2}}(\eta)} \quad \text{(S1-3)}$$

$$L = \left(\frac{k_B}{e}\right)^2 \cdot \left\{ \frac{\left(r+\frac{7}{2}\right) \cdot F_{r+\frac{5}{2}}(\eta)}{\left(r+\frac{3}{2}\right) \cdot F_{r+\frac{1}{2}}(\eta)} - \left[\frac{\left(r+\frac{5}{2}\right) \cdot F_{r+\frac{3}{2}}(\eta)}{\left(r+\frac{3}{2}\right) \cdot F_{r+\frac{1}{2}}(\eta)} \right]^2 \right\} \quad \text{(S1-4)}$$

where S, μ, η, k_B, e, r, R_H, $\hbar$, C_l, E_{def}, and L are the Seebeck coefficient, the carrier mobility, the reduced Fermi level, the Boltzmann constant, the electron charge, the carrier scattering factor (r = -1/2 for acoustic phonon scattering), the Hall coefficient, the reduced plank constant, the elastic constant for longitudinal vibrations, the deformation potential coefficient, and the Lorenz number, respectively. Here:

$$C_l = v_l^2 \cdot \rho \qquad \text{(S1-5)}$$

where v_l is the longitudinal sound velocity and taken as 2730 m·s^{-1} in this study.[5] $F_i(\eta)$ is the Fermi integral expressed as:

$$F_i(\eta) = \int_0^\infty \frac{x^i}{1+e^{(x-\eta)}} dx \qquad \text{(S1-6)}$$

For the effect of Cd-doping on the conduction band of SnSe, **Figure S1** compares the density of state (DOS) of pure SnSe ($Sn_{128}Se_{128}$), Cd-doped SnSe ($CdSn_{127}Se_{128}$) with and without relaxation, respectively. Since Cd has 2 valence electrons less than Sn, the replacing of Sn by Cd should leave out a defect empty band with two holes in the gap. Actually we indeed observed this gap if the Cd atom is not relaxed. But this gap moves to the conduction band after relaxation. This is why Cd does not make any difference to the valence band structure or hole concertation.

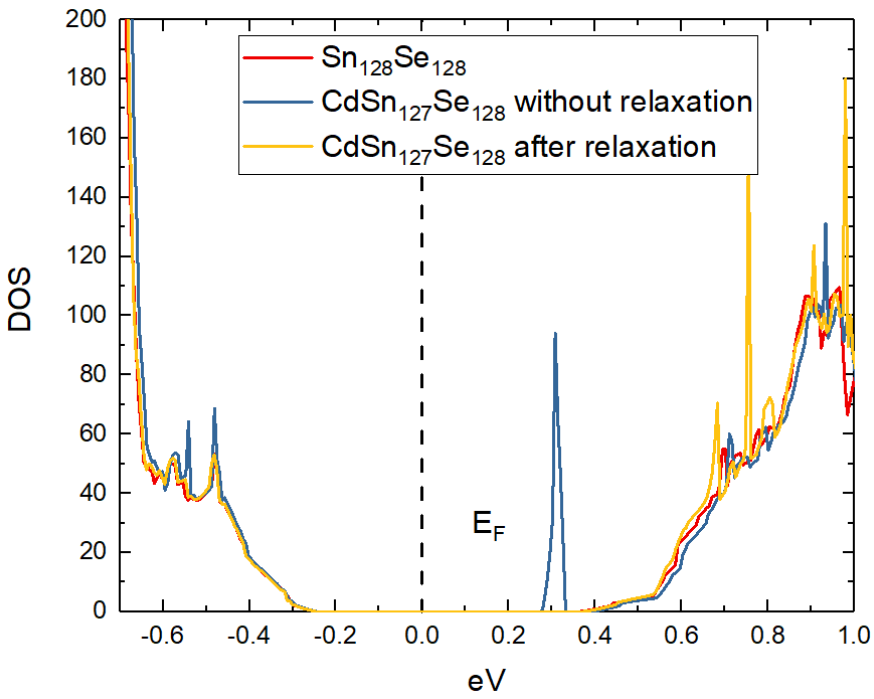

Figure S1. Comparisons of DOS for pure SnSe ($Sn_{128}Se_{128}$), Cd-doped SnSe ($CdSn_{127}Se_{128}$) with and without relaxation.

Section 2. Demonstration of removing CdSe secondary phase.

To demonstrate the CdSe secondary phase can be effectively removed through ultrasonic separation and centrifuging technique after the solvothermal synthesis, we provide detailed XRD patterns of synthesized $Sn_{0.948}Cd_{0.023}Se$ products with CdSe secondary phase derived from the excessive usage of Cd source ($CdCl_2$) during solvothermal synthesis, and pure $Sn_{0.948}Cd_{0.023}Se$ after removing the CdSe secondary phase, respectively, as shown in **Figure S2(a, b)**. It is clear that when achieving $Sn_{0.948}Cd_{0.023}Se$ before removing the CdSe secondary phase, CdSe can be found; after removing the CdSe secondary phase, no CdSe can be found, indicating that high pure SnSe phase can be achieved.

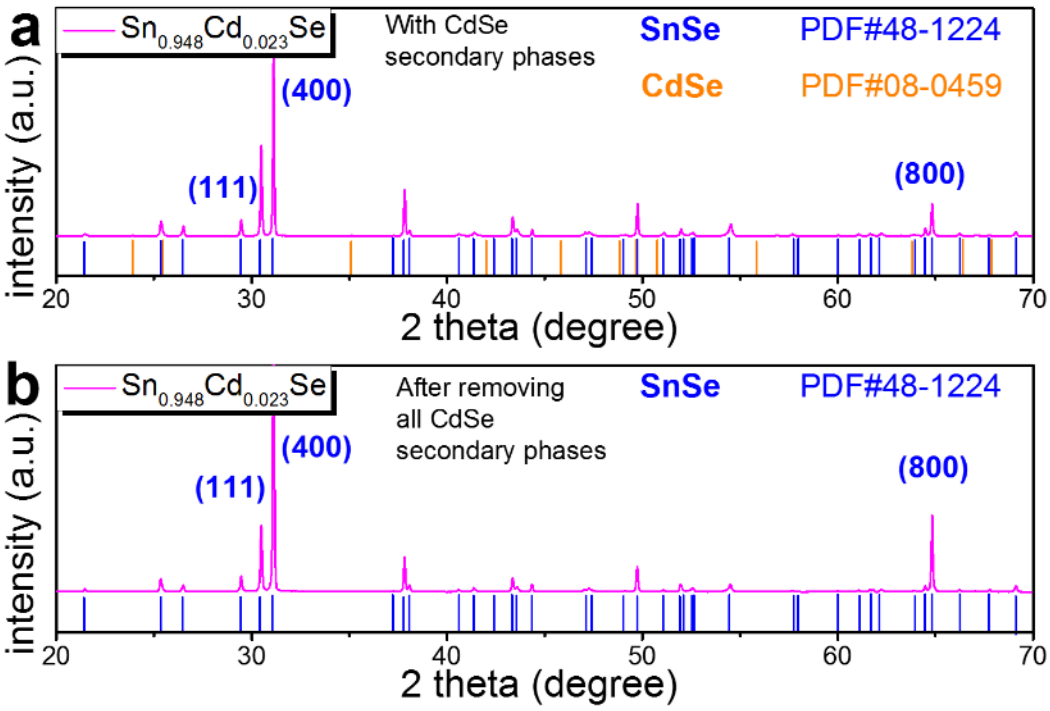

Figure S2. Detailed XRD patterns of synthesized Cd-doped SnSe products ($Sn_{0.948}Cd_{0.023}Se$) with (a) before and (b) after removing CdSe secondary phase.

Section 3. Optical and SEM results for our synthesized pure SnSe products.

Figure S3(a) is an optical image of synthesized pure SnSe powders, which show silver-like metallic lustre. **Figure S3(b)** is their SEM image, from which the pure SnSe have typical rectangular plate-like morphology. **Figure S3(c)** shows a magnified SEM image of SnSe microplate to show the (100) surface with its lateral dimension varies between 30 and 40 μm. Compared with other surfaces, the SnSe microplates possess significant (100) surfaces, which explains why 400* is the strongest peak observed in the XRD results shown in **Figure 4(a)**. **Figure S3(d)** is a magnified SEM image of SnSe microplate to show its lateral surfaces, and the measured thickness of the microplate is ~3.2 μm.

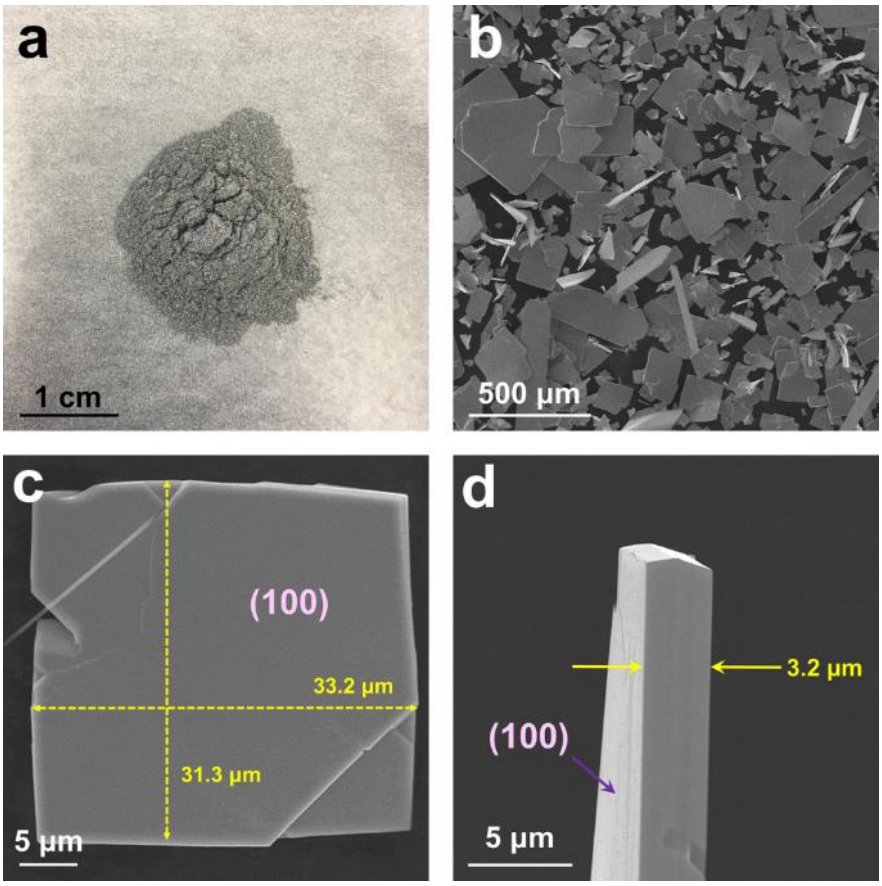

Figure S3. (a) Optical and (b) SEM images of synthesized pure SnSe ($Sn_{0.994}Se$) microplates. (c) Magnified SEM image of one typical $Sn_{0.994}Se$ microplate with (100) surface and (d) magnified SEM image to show the side surfaces.

Section 4. TEM results of pure SnSe products.

For pure SnSe microplate, **Figure S4(a)** shows its TEM image with the plate laid perpendicular to the electron beam. Same to its SEM results, the exterior of microplate showed rough crystal information. **Figure S4(b)** is a magnified TEM image taken from the circled area shown in **Figure S4(a)** to show the edge of microplate, which shows rough lattice. **Figure S4(c)** is the HRTEM image, and **Figure S4(d)** shows corresponding SAED pattern taken along the [100] zone-axis, both indicating that the microplate has typical orthorhombic structure and a (100) surface.

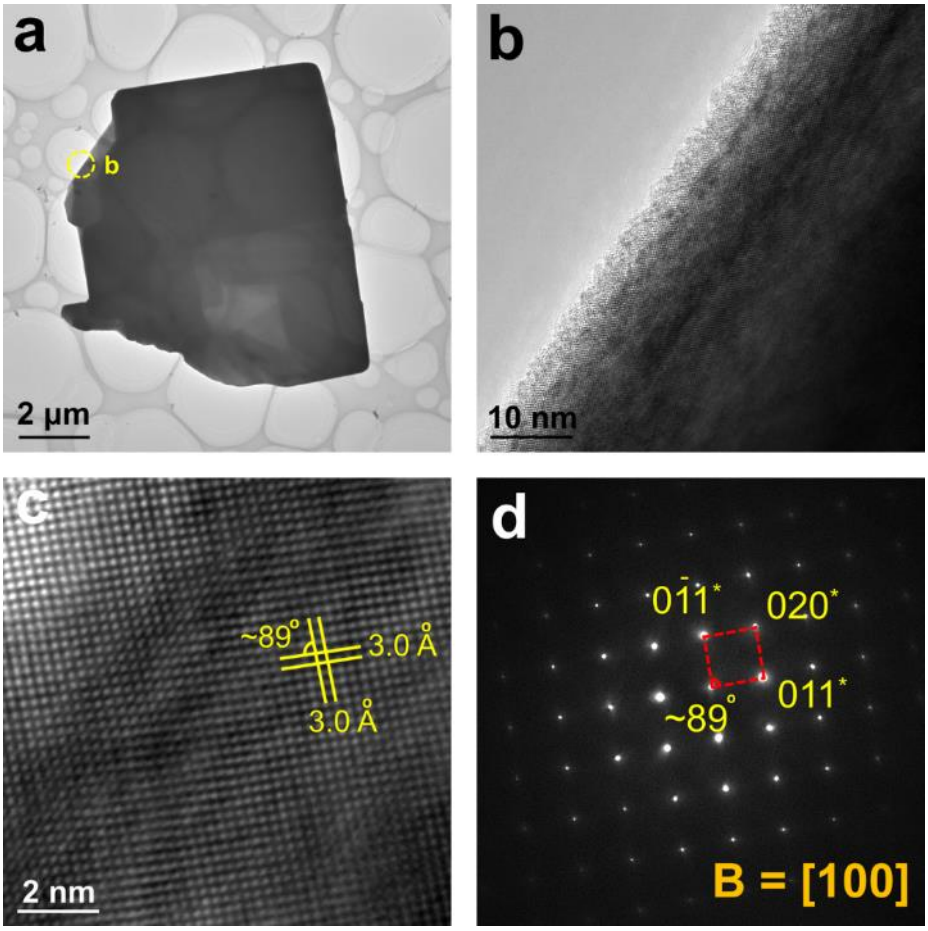

Figure S4. (a) TEM image of one typical pure SnSe ($Sn_{0.994}Se$) microplate; (b) Magnified TEM image of (a); (c) Corresponding HR-TEM image; and (d) SAED pattern.

Section 5. SEM results for our sintered pure SnSe pellets.

To investigate the morphological characteristics of our sintered pure SnSe pellets, detailed SEM investigations were performed. **Figure S5(a, b)** are SEM images of polished surfaces from the ⊥ direction and the // direction, respectively. It is clear that flat surfaces without observable flaw can be achieved, indicating that our sintered pellets have high compact. **Figure S5(c, d)** are SEM images of pellets fractured from the ⊥ direction and the // direction, respectively. The much more distinct fracture features confirm the sintered pellets containing an obvious anisotropy, fitting well with the XRD results shown in **Figure 6(a, b)**.

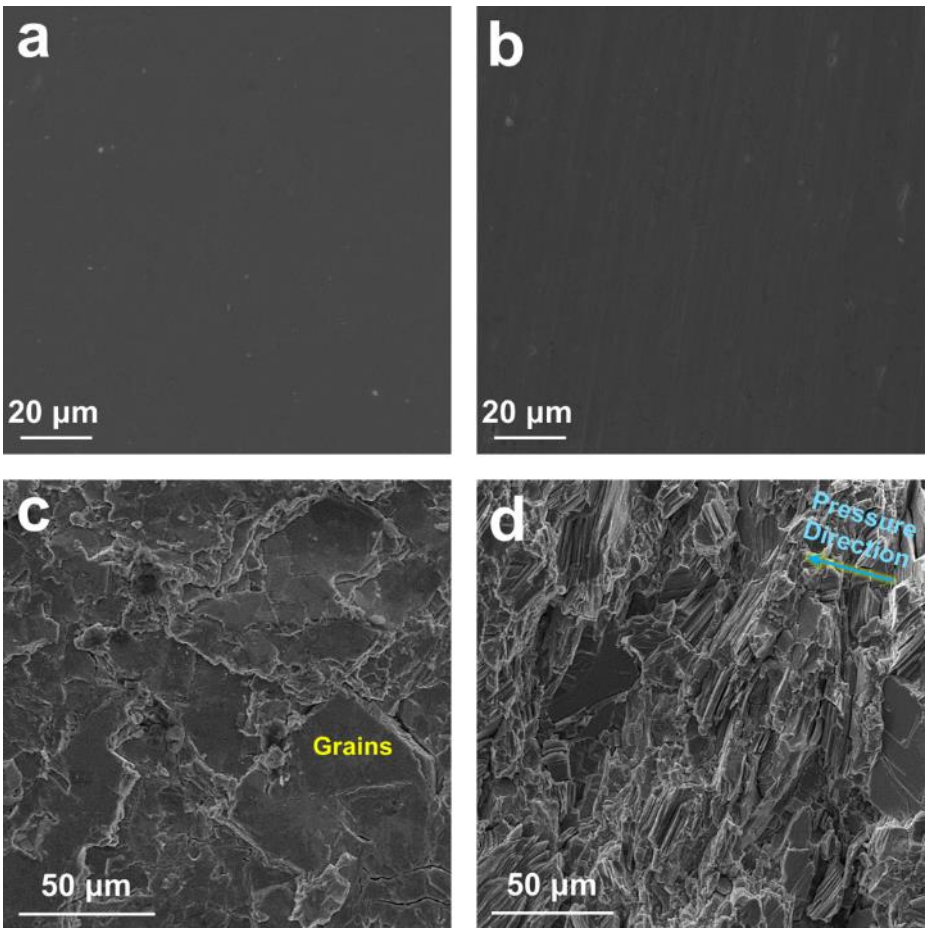

Figure S5. SEM images of pure SnSe pellet ($Sn_{0.994}Se$) polished surfaces from (a) the ⊥ directions and (b) the // directions; SEM images of $Sn_{0.994}Se$ pellet fractured from (c) the ⊥ directions and (d) the // directions.

Section 6. Examination of the reproducibility for obtained thermoelectric properties.

For SnSe, the phase transition between α-SnSe and β-SnSe at 800 K is detrimental to the stability of performance and the mechanical properties. To evaluate the reproducibility of our thermoelectric properties, we measured 6 times for our Cd-doped SnSe pellets ($Sn_{0.948}Cd_{0.023}Se$) from room temperature to 773 K. **Figure S6** shows the *T*-dependent *σ*, *S*, $S^2\sigma$, *κ*, and *ZT* with different measured times. All properties were measured along directions perpendicular to the sintering pressure (⊥ direction). The 1st, 3rd and 5th measurements were taken under heating processes, and the other three measurements were taken under cooling processes. The results indicate that the reproducibility of our obtained thermoelectric properties are high under 773 K.

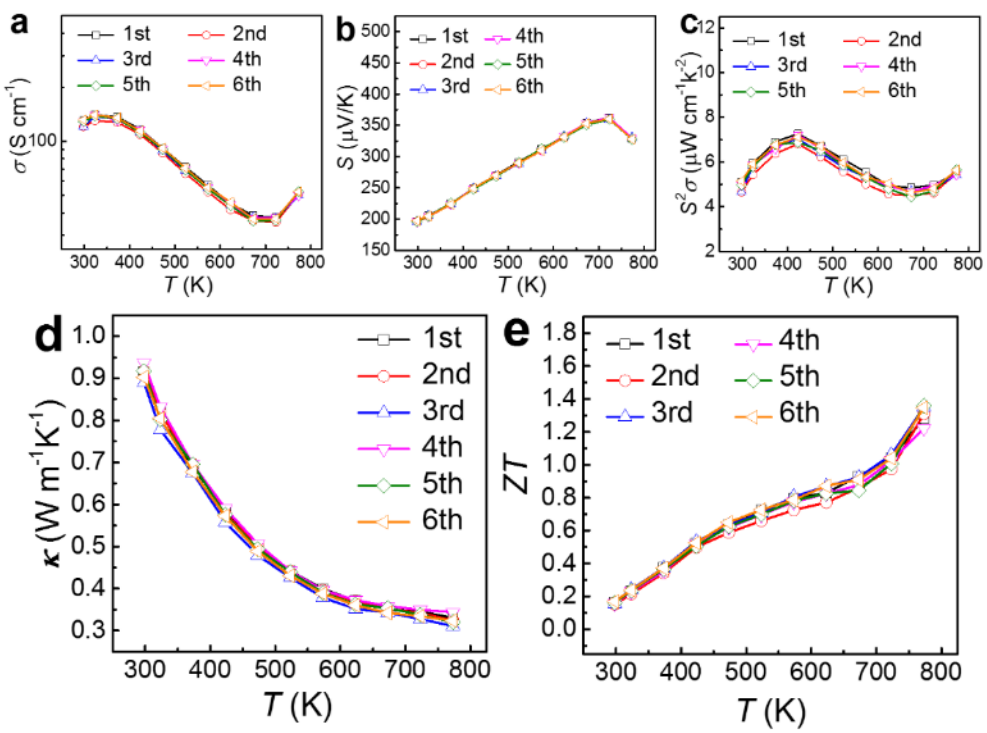

Figure S6. *T*-dependent properties with different measured times for our Cd-doped SnSe pellets ($Sn_{0.948}Cd_{0.023}Se$): (a) σ; (b) S; (c) $S^2\sigma$; (d) κ; and (e) ZT. All properties are measured along ⊥ direction. The 1st, 3rd and 5th measurements were taken under heating processes, and the other three measurements were taken under cooling processes.

Section 7. Examination of the anisotropy for obtained thermoelectric properties.

To evaluate the anisotropy of thermoelectric properties in our pellets, we measured the main properties for both pure SnSe and Cd-doped SnSe ($Sn_{0.948}Cd_{0.023}Se$) pellets with different measured directions from room temperature to 873 K. **Figure S7** shows the plots of measured *T*-dependent properties (σ, S, $S^2\sigma$, κ, and ZT) from our SnSe pellets. The measured direction perpendicular to the sintering pressure is labelled as "⊥", and the measured direction parallel to the sintering pressure is labelled as "//". The results indicate that $Sn_{0.948}Cd_{0.023}Se$ pellets possess stronger anisotropy than their pure counterparts, fitting well with the XRD results shown in **Figure 6(a, b)**.

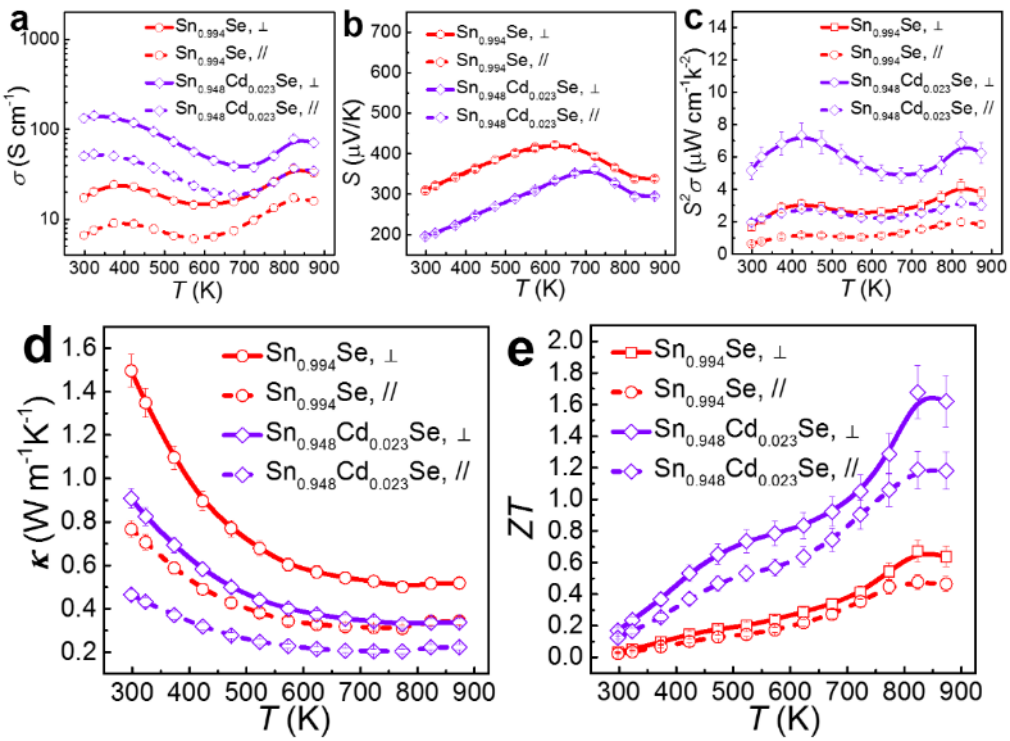

Figure S7. Plots of T-dependent properties with different measured directions from our Cd-doped SnSe pellets: (a) σ; (b) S; (c) $S^2\sigma$; (d) κ; and (e) ZT. The measured directions perpendicular to the sintering pressure is labelled as "⊥", and the measured directions parallel to the sintering pressure is labelled as "//".

Section 8. Measured thermal diffusivities and calculated effective mass, Lorenz number and phonon transport occupation for Cd-doped SnSe pellets.

The measured T-dependent thermal diffusivity (D) for our Cd-doped SnSe pellets are shown in **Figure S8(a)**. Meanwhile, the calculated T-dependent effective mass (m*) and Lorenz number (L) for our Cd-doped SnSe pellets are shown in **Figure S8(b, c)**, respectively. It is clear that the m* slightly increase with increasing the amount of cation vacancy. For L, the values for all samples are stable with the entire temperature range (~1.5×10^{-8} V^2 K^{-2}), indicating that SnSe is a typical thermoelectric material that the κ are significantly depended on phonon scattering. The calculations were based on the SPB model discussed in **Section 1**. Besides, the calculated T-dependent κ_l/κ ratio is shown in **Figure S8(d),** from which more than ~70 % of κ were derived from the phonon transport (κ_l) when T < 873 K, indicating κ is dominated by phonon transport.

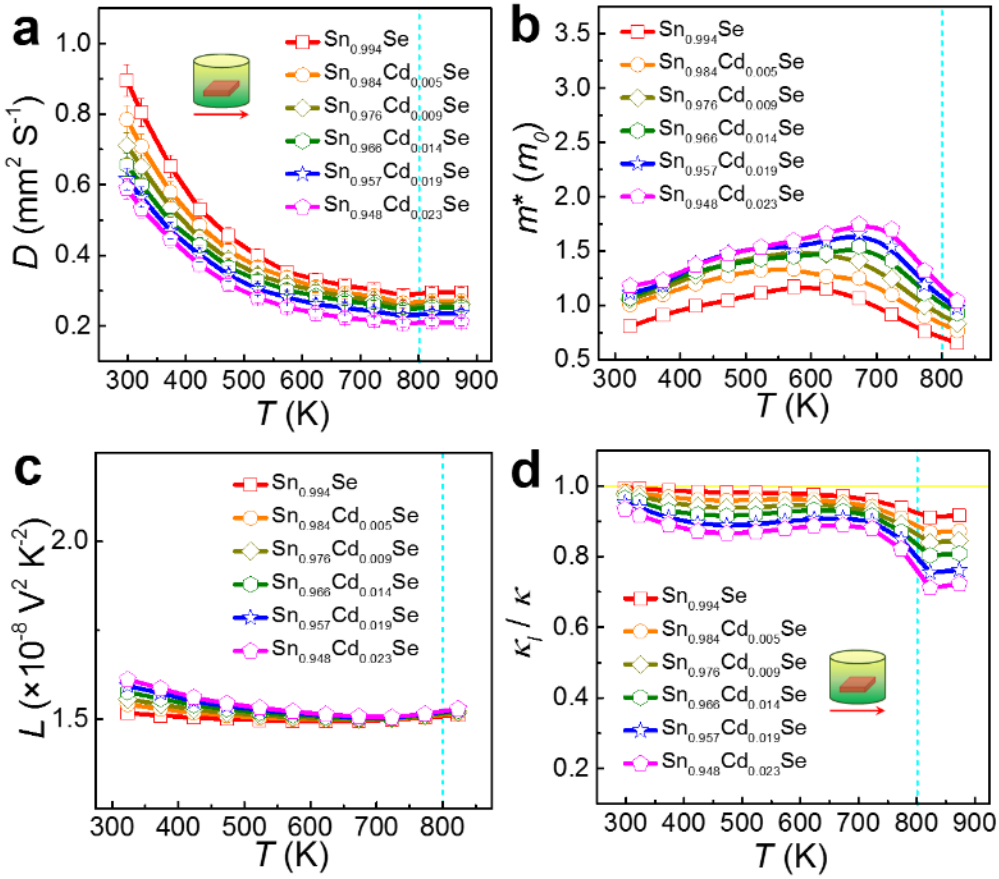

Figure S8. Plots of *T*-dependent (a) *D*; (b) *m**; (c) *L*; and (d) κ_l/κ ratio.

Section 9. Experimental Section.

Reagents and Synthesis. Single crystal Cd-doped SnSe microplates were solvothermally synthesized using Na_2SeO_3 (99.99 %), $SnCl_2{\cdot}2H_2O$ (99.99 %), $CdCl_2$ (99.99 %), ethylene glycol anhydrous (EG, $C_2H_6O_2$, 99.8 %), and NaOH (99.99 %) as precursors (all purchased from Sigma-Aldrich Co. LLC). For the chemical reactions, EG acted as both the solvent and the reducing agent, which can be expressed as:[6]

$$SnCl_2{\cdot}2H_2O \xrightarrow{C_2H_6O_2} Sn^{2+} + 2Cl^- + 2H_2O \qquad \text{(S9-1)}$$

$$Na_2SeO_3 \xrightarrow{C_2H_6O_2} 2Na^+ + SeO_3^{2-} \qquad \text{(S9-2)}$$

$$SeO_3^{2-} + C_2H_6O_2 \rightarrow Se + C_2H_2O_2 + H_2O + 2OH^- \qquad \text{(S9-3)}$$

$$CdCl_2 \xrightarrow{C_2H_6O_2} Cd^{2+} + 2Cl^- \quad \text{(S9-4)}$$

and NaOH was used to adjust the environment of solvent (*pH*), benefited the ion reaction of [6-8]:

$$Se + Sn^{2+} \rightarrow Se^{2-} + Sn^{4+} \quad \text{(S9-5)}$$

$$xSn^{2+} + yCd^{2+} + Se^{2-} \rightarrow Sn_xCd_ySe. \text{ (Not balanced)} \quad \text{(S9-6)}$$

In a typical synthesis, Na_2SeO_3, $SnCl_2{\cdot}2H_2O$ and $CdCl_2$ were dissolved in EG (45 ml), and then added NaOH, kept stirring for 15 min at room temperature. The solution was then sealed in a 125 ml polytetrafluoroethylene-lined stainless steel autoclave. The autoclave was heated in an oven at 230 °C for 36 h, followed by naturally cooled to room temperature. The synthesized products were collected by centrifugation and washed by ethanol and deionized water for several times before drying in the oven at 60 °C for 12 h.

Sintering and Thermoelectric Properties Measurements. To measure their thermoelectric properties, the synthesized products were sintered by SPS (SPS-211Lx, Fuji Electronic Co., Ltd.) at 573 °C for 5 min with a pressure of 60 MPa to form disc-shaped pellets with a dimension of Φ = 12.6 mm and h = 8.0 mm. The densities (ρ) of the sintered pellets were measured by the Archimedes method.[9] In our measurements, σ and S were measured simultaneously using a Seebeck coefficient/electric resistivity measuring system (ZEM-3, ULVAC Technologies, Inc.) in the temperature range between 300 and 873 K. The thermal diffusivity D was measured using the laser flash diffusivity method (LFA 457, NETZSCH Group). κ was calculated using $\kappa = D{\cdot}C_p{\cdot}\rho$,[10] where C_p is the specific heat capacity obtained by differential scanning calorimetry (DSC 404 C; NETZSCH Group), and hole carrier concentration p was measured using the van der Pauw technique under a reversible magnetic

field of 1.5 T. To ensure the repeatability of synthesized products and their demonstrated thermoelectric properties, each pellet are measured for at least 3 times.

Characterizations. The synthesized products were characterized by XRD (Bruker-D8) to determine their crystal structures, and XPS (Kratos Axis Ultra) to determine the existence and amount of Cd in SnSe. The lattice parameters were obtained by analyzing the diffraction patterns with the JADE software package. The morphological characteristics of both synthesized products and sintered pellets were investigated using SEM (JSM-6610, JEOL Ltd.), and their structural and chemical characteristics were studied using HRTEM (TECNAI-F20) and Cs-corrected HR-STEM (Titan-G2). The TEM specimens of sintered specimens were prepared by both focused ion beam technique (FEI Scios Dual-beam System) and slicing the sample using Ultramicrotone. The EPMA (JEOL JXA-8200) was used to determine their compositions, and the EDS (installed in TECNAI-F20) was used to identify the distribution of the elements. The instrumental error of EMPA is 0.1 %. There were 12 test areas for each sample.

DFT calculations. Density functional theory calculations were carried out using the Vienna *Ab initio* Simulation Package (VASP)[11, 12] with the projector augmented wave method (PAW)[12] and the generalized gradient approximation of Perdew, Burke and Ernzerhof (GGA-PBE)[13] for the electronic exchange-correlation functionals. The plane-wave energy cutoff is 450 eV. The SnSe unit cell was relaxed with a 6×18×18 Γ-centered k-mesh, and the convergence thresholds of the total energy and the forces on each atom are 10^{-8} eV and 10^{-6} eV $Å^{-1}$, respectively. The relaxed lattice constants are $a = 11.7615$ Å, $b = 4.2062$ Å, and $c = 4.5475$ Å. With Cd defects and Sn vacancies at different concentrations, we constructed 2×4×4 (256 atoms) and 2×5×5 (400 atoms) supercells. The atoms in supercells were relaxed with 3×3×3 Γ-centered k-mesh until the forces of each atom are smaller than 10^{-3} eV $Å^{-1}$. The densities of states were calculated by using 3×3×3 Γ-centered k-mesh with the tetrahedron

smearing method. The band structures along high-symmetry directions were calculated by using Gaussian smearing method.

Reference

[1] Y. Xu, W. Li, C. Wang, J. Li, Z. Chen, S. Lin, Y. Chen, Y. Pei, *J. Mater. Chem. A* **2017**, *5*, 19143-19150.

[2] J. Shen, Z. Chen, S. lin, L. Zheng, W. Li, Y. Pei, *J. Mater. Chem. C* **2016**, *4*, 209-214.

[3] X. She, X. Su, H. Du, T. Liang, G. Zheng, Y. Yan, R. Akram, C. Uher, X. Tang, *J. Mater. Chem. C* **2015**, *3*, 12116-12122.

[4] L. Zhao, S.M.K.N. Islam, J. Wang, D.L. Cortie, X. Wang, Z. Cheng, J. Wang, N. Ye, S. Dou, X. Shi, L. Chen, G.J. Snyder, X. Wang, *Nano Energy* **2017**, *41*, 164-171.

[5] Y. Xiao, C. Chang, Y. Pei, D. Wu, K. Peng, X. Zhou, S. Gong, J. He, Y. Zhang, Z. Zeng, L.-D. Zhao, *Phys. Rev. B* **2016**, *94*, 125203.

[6] Y. Li, F. Li, J. Dong, Z. Ge, F. Kang, J. He, H. Du, B. Li, J.-F. Li, *J. Mater. Chem. C* **2016**, *4*, 2047-2055.

[7] Z.-H. Ge, K. Wei, H. Lewis, J. Martin, G.S. Nolas, *J. Solid State Chem.* **2015**, *225*, 354-358.

[8] C. Wang, Y. Li, G. Zhang, J. Zhuang, G. Shen, *Inorg. Chem.* **2000**, *39*, 4237-4239.

[9] X. Shi, Z. Chen, W. Liu, L. Yang, M. Hong, R. Moshwan, L. Huang, J. Zou, *Energy Storage Mater.* **2018**, *10*, 130-138.

[10] L.D. Zhao, S.H. Lo, Y. Zhang, H. Sun, G. Tan, C. Uher, C. Wolverton, V.P. Dravid, M.G. Kanatzidis, *Nature* **2014**, *508*, 373-377.

[11] G. KresseJ. Hafner, *Phys. Rev. B* **1993**, *47*, 558.

[12] G. KresseJ. Furthmüller, *Phys. Rev. B* **1996**, *54*, 11169.

[13] J.P. Perdew, K. Burke, M. Ernzerhof, *Phys. Rev. Lett.* **1996**, *77*, 3865.